

ABSTRACT

Title of Dissertation: TIME-TEMPERATURE DEPENDENT
CHARACTERIZATION OF POLYMERS FOR
ACCURATE PREDICTION OF STRESSES IN
ELECTRONIC PACKAGES

Hyun Seop Lee, Doctor of Philosophy, 2021

Dissertation directed by: Professor Bongtae Han
Department of Mechanical Engineering

Epoxy molding compound (EMC) is a thermosetting polymer filled with inorganic fillers such as fused silica. EMC has been used extensively as a protection layer in various semiconductor packages. The warpage and the residual stress of packages are directly related to the thermomechanical properties of EMC. As the size of semiconductor packages continues to shrink, prediction of the warpage and residual stress becomes increasingly important. The viscoelastic properties of EMC are the most critical input data required for accurate prediction. In spite of the considerable effort devoted to warpage prediction, accurate prediction of warpage remains a challenging task. One of the critical reasons is the inappropriate assumption about the bulk modulus – time and temperature “independent” bulk modulus, which is not valid at high temperatures.

In this thesis, a novel experimental method, based on an embedded fiber Bragg grating (FBG) sensor, is developed and implemented to measure a complete set of

linear viscoelastic properties of EMC just from a single configuration. A single cylindrical EMC specimen is fabricated, and it is subjected to constant uniaxial compression and hydrostatic pressure at various temperatures. Two major developments to accommodate the unique requirements of EMC testing include: (1) a large mold pressure for specimen fabrication; and (2) a high gas pressure for hydrostatic testing while minimizing a temperature rise. The FBG embedded in the specimen records strain histories as a function of time. Two linear viscoelastic properties, Young's modulus and Poisson's ratio, are first determined from the strain histories by the analytical relationship between the BW change and the properties. A unique sequential iterative procedure is proposed to completely negate the effect of measurement uncertainties during complex non-linear regression. The other two elastic properties, Shear modulus and Bulk modulus, are also calculated from the relationship among the linear elastic constants. The master curves are produced, and the corresponding shift factors are determined.

Validity of three major assumptions associated with the linear viscoelasticity - thermorheological simplicity, Boltzmann superposition and linearity - are verified by supplementary experiments. The effect of the time-dependent bulk modulus on the warpage is also discussed.

TIME-TEMPERATURE DEPENDENT CHARACTERIZATION OF POLYMERS FOR
ACCURATE PREDICTION OF STRESSES IN ELECTRONIC PACKAGES

By

Hyun Seop Lee

Dissertation submitted to the Faculty of the Graduate School of the
University of Maryland, College Park, in partial fulfillment
of the requirements for the degree of
Doctor of Philosophy
2021

Advisory Committee:
Prof. Bongtae Han, Chair/Advisor
Prof. Abhijit Dasgupta
Prof. Patrick McCluskey
Prof. Peter A. Sandborn
Prof. Sung W. Lee

© Copyright by

Hyun Seop Lee

2021

Acknowledgements

I have been helped by many people throughout my PhD study. Although I cannot not mention everyone who helped me throughout this journey, I'd like to express my gratitude to a few of them who have been particularly helpful and inspiring.

First, I would like to express my sincere thanks to my advisor, Dr. Bongtae Han, for giving the opportunity to work with him. I'm really grateful for the huge amount of time he spent for me to guide and inspire me. I learned a lot from him not only academically but also personally. It was not an easy journey to pursue PhD, and I know that this would not be possible without Dr. Han's understanding and guidance. I'm sure that the valuable lectures and guidance he gave me will be greatly helpful not only for my career but also for my life in general.

Next, I would like to thank our LOMSS members. I thank Sukrut and Ryan for their cooperation and assistance with my experiments. Dae-Suk, Bulong, Sean, Yong, Byung and Jack are also greatly appreciated for their support and company during my PhD journey.

I would like to thank the members of my dissertation committee, Dr. Abhijit Dasgupta, Dr. Patrick McCluskey, Dr. Peter Sandborn and Dr. Sung Lee. I really appreciate their valuable comments during my defense.

Most importantly, I wish to express my gratitude to my parents. I could not finish it without their support and their trust in me. I also thank my beloved girlfriend, Gil-ah, for years of her patience and support. I will do my best to give back all of it.

Table of Contents

| | |
|---|------------|
| Acknowledgements | ii |
| Table of Contents | iii |
| List of Figures..... | v |
| Chapter 1 Background | 1 |
| 1.1. Epoxy Molding Compounds for Semiconductor Packages | 1 |
| 1.2. Thermomechanical Analysis of Packages and EMC Characterization . | 7 |
| 1.3. Motivation and Objective | 11 |
| Chapter 2 Literature Review | 13 |
| 2.1. Background..... | 13 |
| 2.2. Thermomechanical Behavior of Polymers | 14 |
| 2.2.1. Cure Shrinkage and Modulus Evolution of Polymeric Materials. | 14 |
| 2.2.2. Coefficient of Thermal Expansion and Glass Transition Temperature | 18 |
| 2.2.3. Viscoelasticity of Polymers | 21 |
| 2.2.4. Linear Viscoelasticity and Boltzmann Superposition Principle (BSP) | 25 |
| 2.2.5. Thermorheologically Simple (TRS) and Time-Temperature Superposition | 30 |
| 2.3. Fiber Bragg Grating as a Sensor | 32 |
| Chapter 3 Time dependent Property Measurements by FBG Embedded Specimen | 36 |
| 3.1. Specimen Configuration and Governing Equations | 36 |
| 3.2. Sequential Iterative Procedure to Obtain Two Constants | 41 |
| 3.3. Master Curves Under Creep and Stress Relaxation..... | 48 |
| Chapter 4 Development of the Testing Setup for the Proposed Method | 51 |
| 4.1. Specimen Fabrication | 51 |

| | |
|---|-----------|
| 4.2. Uniaxial Test Setup..... | 53 |
| 4.3. Hydrostatic Test Setup..... | 62 |
| Chapter 5 Measurement Result of Two Time Dependent Elastic Moduli..... | 66 |
| Chapter 6 Effect of Constant Bulk Modulus and Poisson’s ratio on Thermal Stress Analysis..... | 77 |
| 6.1. Effect of Time-dependent Bulk Modulus on Reliability Assessment of Automotive Electronic Control Unit..... | 77 |
| 6.2. Effect of Constant Poisson’s ratio on Warpage Analysis | 82 |
| 6.2.1. Polymer Layer Sandwiched by Rigid Plates..... | 83 |
| 6.2.2. Wirebond Ball Grid Array (BGA) Package..... | 85 |
| Chapter 7 Conclusion and Future Work | 89 |
| 7.1. Conclusion | 89 |
| 7.2. Future Work..... | 90 |
| Reference | 91 |

List of Figures

| | |
|--|----|
| Figure 1.1 Cross-section image of EMC [1]..... | 1 |
| Figure 1.2 Packages using EMC; (a)lead frame and (b) BGA package [8]..... | 2 |
| Figure 1.3 Schematic description of transfer molding process..... | 3 |
| Figure 1.4 Schematic description of compression molding process [12] | 4 |
| Figure 1.5 Schematic comparison between (a) conventional BGA and (b) FO-WLP packages | 5 |
| Figure 1.6 (a) CUF and (b) MUF [17] | 6 |
| Figure 1.7 Schematic description of effect of warpage on interconnection; (a)lead frame and (b) BGA package | 8 |
| Figure 2.1 Repeating structure examples of thermoplastic polymers; (a) polyethylene and (b) polycarbonate [45] | 13 |
| Figure 2.2 Repeating structure of examples of thermoset polymers; (a) Polyurethane and (b) epoxy based polymers [45] | 14 |
| Figure 2.3 Illustration of property evolution in a typical polymer system [61]..... | 15 |
| Figure 2.4 Illustration of CTE and T_g measurement using TMA | 20 |
| Figure 2.5 Arrhenius relationship | 22 |
| Figure 2.6 Stress relaxation test: (a) strain input and (b) stress output..... | 23 |
| Figure 2.7 Creep test: (a) stress input and (b) strain output..... | 24 |
| Figure 2.8 Stress relaxation test (a), isochronous stress-strain relationship (b), and normalized stress of stress relaxation test results of material with linear viscoelastic behavior | 27 |
| Figure 2.9 Boltzmann superposition principle example | 28 |
| Figure 2.10 Description of time-temperature superposition..... | 31 |
| Figure 2.11 Illustration of an FBG spectrum reflection and transition [4] | 32 |
| Figure 3.1 FBG embedded in the Cylindrical Specimen | 36 |
| Figure 3.2 Schematic of a polymer specimen with embedded FBG under axial and radial loading | 37 |

| | |
|--|----|
| Figure 3.3 Analytical solution verification for σ_{rr} and σ_{zz} within a FBG embedded specimen..... | 40 |
| Figure 3.4 stress (a) σ_{zz} and (b) σ_{rr} of the FBG when a specimen is subjected to a uniaxial compression loading..... | 42 |
| Figure 3.5 BW change under uniaxial loading as a function of (a) E_p and (b) ν_p | 44 |
| Figure 3.6 Example Young's modulus and Poisson's ratio..... | 45 |
| Figure 3.7 Generated BW change..... | 46 |
| Figure 3.8 Obtained (a) Young's modulus and (b) Poisson's ratio by the sequential iterative procedure..... | 47 |
| Figure 3.9 Error of the sequential iterative procedure..... | 48 |
| Figure 3.10 Schematic description of shifting algorithm..... | 49 |
| Figure 3.11 $E(t)$ obtained from convolution of $E_{crp}(t)$ | 50 |
| Figure 4.1 Mold assembly to fabricate the EMC specimen..... | 51 |
| Figure 4.2 Setup for specimen fabrication..... | 52 |
| Figure 4.3 Schematic of the uniaxial test setup..... | 53 |
| Figure 4.4 Uniaxial testing setup when (a) heating chamber is open and lifted for setting up and (b) heating chamber is closed and in place for the testing..... | 54 |
| Figure 4.5 (a) Insulation layers of the insulation cover and (b) insulation cover covering entire heated parts of the testing setup..... | 56 |
| Figure 4.6 Testing heating capability to confirm the temperature uniformity within the specimen..... | 57 |
| Figure 4.7 Fastest loading from the setup..... | 58 |
| Figure 4.9 Long term loading stability test..... | 59 |
| Figure 4.10 BW changes normalized by the applied uniaxial compressive stress at (a) 25 °C, (b) 125 °C and (c) 175 °C..... | 61 |
| Figure 4.11 Reflected signal spectrum before and after the x..... | 61 |
| Figure 4.12 Hydrostatic Test Setup..... | 62 |
| Figure 4.13 Compression sealing for the optical fiber..... | 63 |

| | |
|--|----|
| Figure 4.14 BW changes normalized by the applied hydrostatic stress at (a) 25 °C, (b) 125 °C and (c) 175 °C | 65 |
| Figure 5.1 Raw Bragg wavelength change from uniaxial creep test | 67 |
| Figure 5.2 Raw Bragg wavelength change from hydrostatic creep test | 67 |
| Figure 5.3 Compliance at various temperatures and shifted to obtain shift factors.... | 68 |
| Figure 5.4 Shift factors obtained from shifting compliance | 69 |
| Figure 5.5 Compressibility at each temperature shifted using shift factors obtained from compliance result..... | 69 |
| Figure 5.6 Creep compliance fitted into a functional form..... | 70 |
| Figure 5.7 Creep compressibility fitted into a functional form | 71 |
| Figure 5.8 Shift factors fitted into (a) single WLF function and (b) piece-wise Shift functions | 74 |
| Figure 5.9 Master curve of four time-dependent constants (reference temperature: 115 °C)..... | 75 |
| Figure 6.1 Implication of the assumption of bulk modulus behavior: (a) temperature-independent; and (b) time-independent | 78 |
| Figure 6.2 (a) Wirebond “lift-off” failure in a DPAK, and (b) Al wire bond interface of interest [9]..... | 79 |
| Figure 6.3 Schematic cross-sectional view of the FEA model to simulate the presence of the outer mold [9]..... | 79 |
| Figure 6.4 FEA models of DPAK in ECU unit shown (a) with EMC (b) without EMC | 80 |
| Figure 6.5 Comparison of wire bond interface stresses (a) without the constant bulk modulus assumption and (b) with the assumption | 81 |
| Figure 6.6 Axisymmetric structure containing three layers of discs and (b) the corresponding 2–D axisymmetric model..... | 84 |
| Figure 6.7 Axial stress along the interface..... | 84 |
| Figure 6.8 Maximum opening stress as a function of Poisson's ratio of Material 2... | 85 |
| Figure 6.9 Cross-sectional view of the package | 86 |

| | |
|---|----|
| Figure 6.10 Quarter symmetric model of the package (a) geometry without EMC and (b) actual FEM mesh | 86 |
| Figure 6.11 (a) Deformed configuration of the package and (b) the z displacement along the diagonal direction | 87 |
| Figure 6.12 Warpage of the wire bond package as a function of Poisson's ratio of EMC | 88 |

Chapter 1 Background

1.1. Epoxy Molding Compounds for Semiconductor Packages

Epoxy molding compound (EMC) is an epoxy resin filled with inorganic fillers such as fused silica. Figure 1.1 shows the cross section of EMC material. It also contains other chemicals such as curing agents, mold release agents, etc. Inorganic fillers and other agents are added to the epoxy resin to achieve required characteristics for the application.

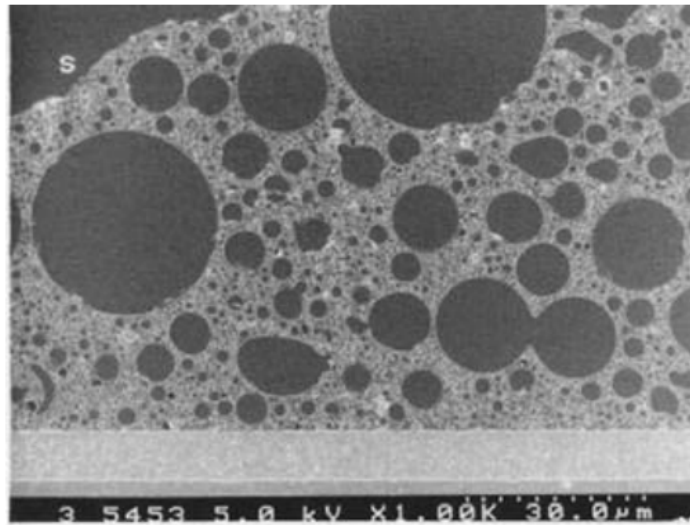


Figure 1.1 Cross-section image of EMC [1]

EMC has been used extensively for encapsulation to provide a protection layer in semiconductor packages, including traditional lead frame packages as well as advanced packages [2, 3]. Figure 1.2 shows a few examples of packages encapsulated with EMC. It is used to protect the chip and interconnection from the ambient environment (e.g., moisture, heat, and shock) and provide proper electrical insulation. Epoxy resin is preferred because it is easier to process and has lower cure shrinkage,

higher electrical resistance, better heat, chemical and moisture resistance compared to other polymers [4-7].

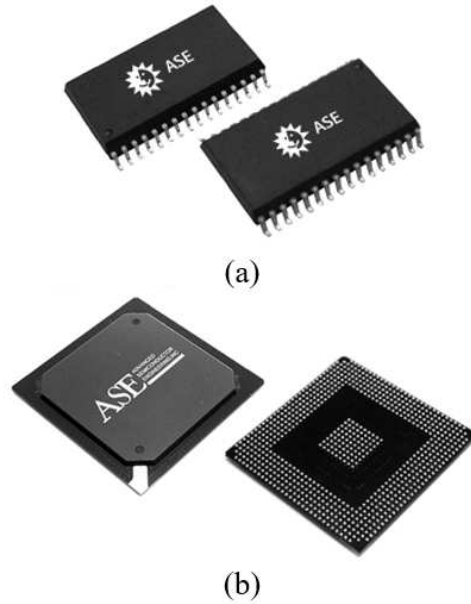


Figure 1.2 Packages using EMC; (a) lead frame and (b) BGA package [8]

Transfer molding process has been widely used for encapsulating packages with EMC [9-11]. Figure 1.3 portrays the transfer molding process for wire bond ball grid array (BGA) packages. In the transfer molding process, uncured EMC preformed in a pellet shape is first placed in a reservoir at the preheating temperature. The preheating temperature is the temperature high enough to melt the preformed pellet of uncured EMC, but it is lower than the temperature at which rapid curing of EMC occurs.

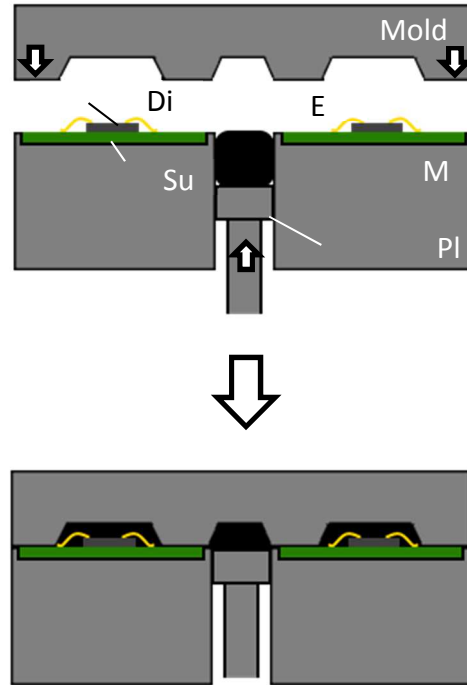


Figure 1.3 Schematic description of transfer molding process

After the EMC becomes liquid with high viscosity, the EMC is injected into the package mold by a high pressure. An example pressure and temperature for this process which has been used widely is around 7 MPa and 175 °C, respectively. After the EMC is cured enough to be considered as a solid, it is released from the mold. The duration of this process can be as short as a couple of minutes. Released products are placed into a high temperature environment which is the same or similar to the mold curing temperature. This process, which takes relatively longer up to several hours, is called the post mold curing process (PMC), and is done to ensure the EMC is completely cured.

Compression molding process is used for advanced packages such as fan-out wafer level packages (FO-WLP) in which transfer molding process cannot be used to apply EMC to the package [12]. Conventional transfer molding process is not

applicable for fan-out wafer level packages because it is manufactured on the wafer level, where multiple dies are placed, and interconnections are formed.

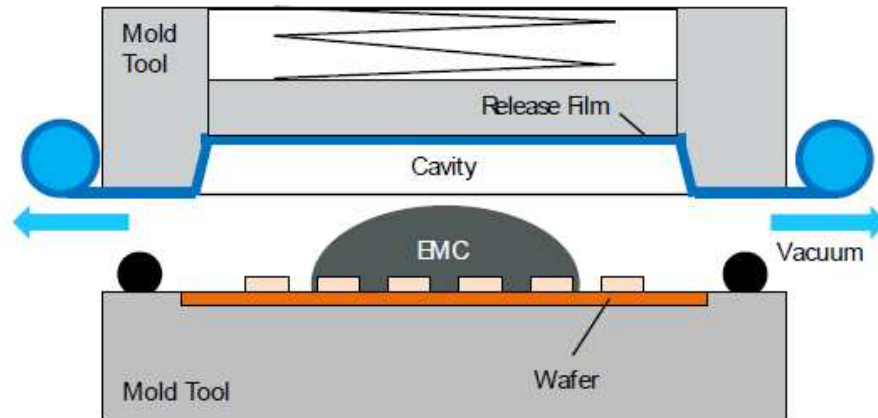
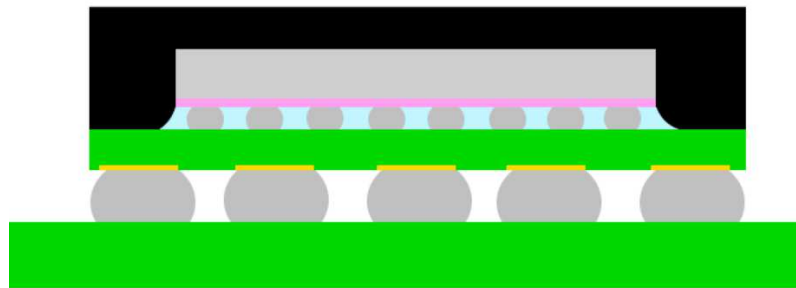


Figure 1.4 Schematic description of compression molding process [12]

Figure 1.4 shows the schematic diagram of compression molding process. Instead of being injected into the mold with high pressure as in transfer molding, uncured EMC materials in various forms are dispensed in the middle of the mold cavity and flow during the compression to fill the cavity.

Compression molding is done at vacuum under high temperature and pressure to ensure complete homogeneous encapsulation without voids or trapped air. This molding process can be performed either on wafer or panel level, depending on the application. Uncured EMC used for compression molding can be in various forms including liquid, granular (powder), or sheet [12-14]. Compression molding process also utilizes the post molding process which is the same with that of transfer molding process after it is released from the compression mold. FO-WLP is one of the important emerging packaging technologies because of its features such as thin form factor due to substrate-less structure, low impedance, and high input/output (I/O) number density. FO-WLP does not use substrates, on which dies are attached to as in conventional BGA

packages using solder bumps. Instead, FO-WLP uses a redistribution layer (RDL) to provide interconnections, which are formed on the die and EMC surface directly.[12, 15, 16]



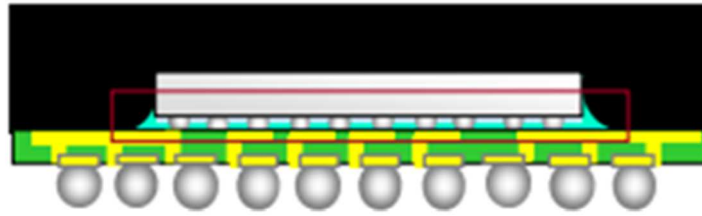
(a)



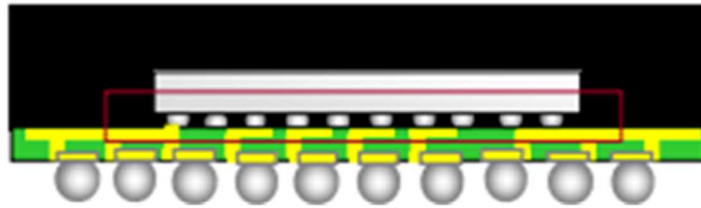
(b)

Figure 1.5 Schematic comparison between (a) conventional BGA and (b) FO-WLP packages

Figure 1.5 illustrates difference between conventional flip chip BGA packages and FO-WLP. Therefore, EMC serves an extended role as a mechanical structure on which the interconnections are formed instead of being a protective layer applied over the substrate and the chip after all the interconnections are formed. Because of EMC's fundamental role in FO-WLP, it is becoming more important to understand the behavior of the EMC accurately compared to the conventional package types.



(a)



(b)

Figure 1.6 (a) CUF and (b) MUF [17]

Another technology where EMC plays a larger role than its previous function as a simple protection layer is in molded underfill (MUF). MUF provides lower material cost and higher throughput compared to conventional capillary underfill (CUF) without compromising its reliability. [17-19] MUF utilizes EMC not only as a chip encapsulation, but also as the underfill which will fill the gap between the chip and substrate to reduce stresses on the solder joints. Figure 1.6 shows the schematic difference between packages using CUF and MUF. The molded underfill process offers cost advantage compared to the traditional capillary underfill (CUF) process by reducing the process from two step (underfill and mold) to one step (mold). MUF also enables finer spacing between die-to-die and die-to-passives, which offers another advantage of smaller package size for multichip packages. To be implemented for MUF, the EMC should have smaller filler size to fill all the gap below dies [17] which

can be around 10 μm with advanced packages.[19] Since EMC serves as underfill, it implies that EMC will be directly interact with solder bumps under the die. Therefore, understanding the behavior of EMC is more important when MUF is used to predict the stress within the package and assess solder joints reliability accurately.

1.2. Thermomechanical Analysis of Packages and EMC Characterization

The residual stress and warpage issues are two important mechanical challenges of microelectronics packaging. The residual stress can affect the products' performance by introducing warpage, delamination and even die crack [20-25]. Warpage becomes more and more important in reliability and manufacturing yield as package development advances. Warpage was not very important in early types of packages where only the edges of the packages were utilized for the interconnection. However, warpage started to become more important when the I/O density packages increased, and packages started to utilize its entire area for interconnections as in ball grid array (BGA) packages since it may cause the open or bridge between adjacent solders as illustrated in Figure 1.7. Figure 1.7 shows schematically why the warpage affects the reliability more in BGA than traditional lead frame packages. The JEDEC standard specifies that the coplanarity of the BGA package must be under 6 mils (150 μm) [26]. The warpage issue is becoming more important due to the current trends in industry: a larger package size leading to a large DNP (distance from the neutral point) [27]; green molding compound with higher filler contents [21] and coreless substrate[28].

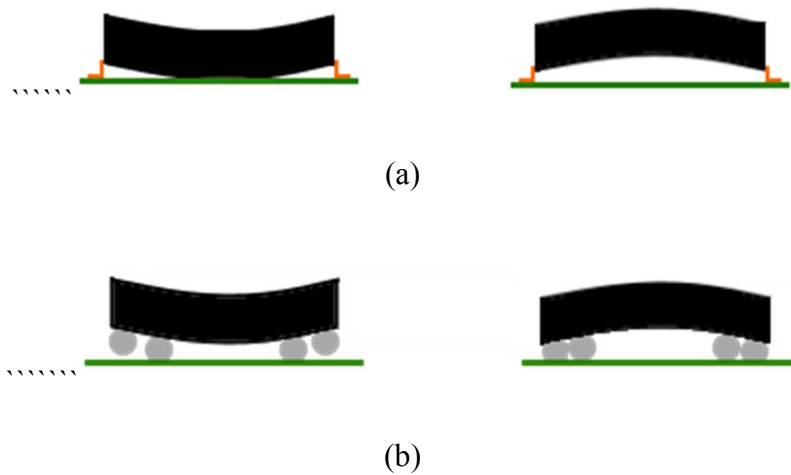


Figure 1.7 Schematic description of effect of warpage on interconnection; (a)lead frame and (b) BGA package

The stresses of advanced semiconductor packages are caused by the difference in CTE between EMC and adjacent materials (e.g., die and solder bumps) [12]. After the EMC is cured in a package, the package itself usually undergoes various temperature excursions such as the reflow process for making interconnections and operation of the device. These temperature excursions cause stress within the package due to the CTE mismatch between different materials within the package. The CTE of EMC is about 10 ppm at low temperature, which is higher than a silicon chip, and increases dramatically at the temperatures higher than the EMC glass transition temperature. In addition, epoxy resin absorbs moisture, and its volume increases when the moisture content increases. This hygroscopic swelling which is the volumetric expansion due to moisture absorption can also cause undesirable stress and warpage within packages.

To minimize undesirable stress caused by epoxy resin, inorganic fillers, typically fused silica, are added to the epoxy resin to achieve lower CTE and lower

moisture absorption. Figure 1.1 shows the cross section of an EMC which clearly containing spherical fused silica fillers. Higher filler content generally lowers the overall resin CTE as fused silica has very low CTE (0.2 ~ 0.5 ppm/°C). The filler content of EMC has been increased to achieve lower CTE. The filler size distribution must be controlled to achieve a very high filler content. Although CTE mismatch can be reduced by increasing filler content, the EMC's Young's modulus will increase proportionally, and high Young's modulus will increase the stress and known as the main factor affects warpage of the packages.[16] Therefore, it is important to understand the behavior of EMC and accurately characterize it to better assess the stress and reliability of advanced semiconductor packages.

EMC contains epoxy resin which is a thermosetting polymer, and it is well known that polymers are viscoelastic at all temperature. Therefore, EMC is a viscoelastic material. [29-32] Characterization of viscoelastic material requires time and temperature dependent measurement of two properties out of Young's modulus, shear modulus, bulk modulus and Poisson's ratio which requires time-consuming effort. Therefore, temperature dependent Young's modulus and Poisson's ratio were often used for thermomechanical analysis of packages.[33-35] To characterize its viscoelastic properties, linear viscoelasticity model has been used and known to be valid for EMC within its typical strain range expected in semiconductor packages. In the linear viscoelasticity regime, two elastic constants in Equation (1.1) have the following relationships with two other elastic constants as [36]:

$$K(t) = \frac{E(t)G(t)}{9G(t) - 3E(t)}, \quad G(t) = \frac{E(t)}{2(1 + \nu(t))} \quad (1.1)$$

where $E(t)$ and $\nu(t)$ are the time-dependent Young's modulus and Poisson's ratio. For predictive modeling, two of the four constants in Eq. (1) must be measured experimentally.

The Young's modulus is relatively easy to measure using dynamic mechanical analyzer. (DMA) There have been several attempts to measure another constant; they include strain gage [36] and moiré interferometry [37] for Poisson's ratio measurement, the dilatometer using a fluid pressure [38, 39] for bulk modulus measurement, and DMA [40] for shear modulus measurement.

DMA has been most widely used for EMC property measurements. The frequency-temperature sweep can be implemented to measure the temperature- and time-dependent modulus [41-43]. Although it is time-consuming, this procedure can be routinely practiced using commercial equipment, but it is usually difficult to obtain elastic constants other than the Young's modulus.

Due to the complexity involved in measuring elastic constants other than the Young's modulus, it has often been assumed that the bulk modulus is "time-independent" [44-47]. This assumption is based on the fact that the traditional viscosity theory were based only on shear motion of the solid [45]. With this assumption, only Young's modulus has to be measured for viscoelastic modelling. This assumption has been widely accepted for thermomechanical analysis of packages because the operating ambient and junction temperature condition (up to 85 °C) for commercial electronics are lower than typical glass transition temperature (around 135 °C) where a large change of properties is expected. Because of the reason, standard accelerated testing

conditions widely used for packages were also lower than the glass transition temperature [48, 49] where no significant change in bulk modulus is expected.

1.3. Motivation and Objective

There are several important applications where temperatures higher than the glass transition temperature must be considered. The most well-known application is the package on package (PoP) [50-52]. PoP is a packaging method to stack two or more BGA packages atop each other with standard interface to route signals between them. It is reported that about 90% of the PoP defects are caused by warpage during solder reflow [53] at which the temperature is much higher than the glass transition temperature. The package stack goes through a single reflow, and thus, it is very important to match the warpage of the top and bottom packages during the reflow. The mismatch of the warpage between the top package and the bottom package at the reflow temperature will easily introduce solder opening or bridging.

Another application where the temperature higher than the glass transition temperature is important is FO-WLP mentioned in the previous section. Unlike other applications where EMC is applied after the interconnection between the die and substrate is formed, the RDL formed directly on EMC. Therefore, the warpage caused by EMC after the molding process which is at the temperature much higher than T_g need to be well controlled and predicted to ensure manufacturing yield. [15, 16, 54] Automotive application is also one of the most important emerging applications of semiconductors nowadays. According to Automotive Electronics Council, the ambient operating temperature of the semiconductor devices for automotive application can be

up to 150 °C for the devices placed under the hood [AEC Q100] and single failure can be fatal in the automotive industry.

For these applications in which thermomechanical analysis over the glass transition temperature is important, using time-independent bulk modulus obviously invalid. Despite of increasing importance of it, the effect of using constant bulk modulus assumption for thermomechanical analysis of packages has not been investigated.

In this study, a novel technique to measure time dependent Young's and bulk modulus using a single specimen configuration with embedded fiber Bragg grating will be developed. Required hardware and software will be developed and measurement will be conducted and the effect of using time-independent bulk modulus will be discussed. Basic concept of viscoelasticity, polymer characteristics and FBG fundamentals utilized in the measurement will be reviewed in chapter 2. Chapter 3 will present the technique to measure Young's modulus and bulk modulus using FBG. The hardware development to implement the technique will be discussed in chapter 4 and the viscoelastic properties of EMC measured using the technique will be presented in chapter 5. The effect of constant bulk modulus assumption in the analysis for an application in which a temperature higher than typical glass transition temperature will be discussed in chapter 6.

Chapter 2 Literature Review

2.1. Background

Polymeric materials are those materials composed of molecules with very high molecular weight. It consists of molecular chains which has repeating unit structure along the chain structure. The repeating structure is also called Mer structure and it determines the characteristic of the polymer. Polymer can be classified in many ways, but most polymers can be broadly classified as either thermoplastics or thermosetting polymers.

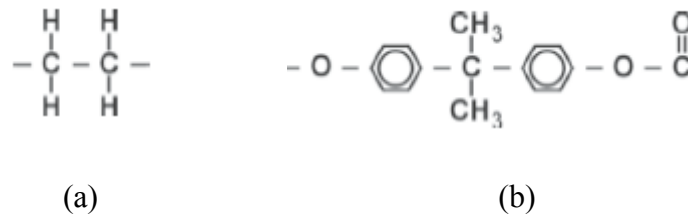
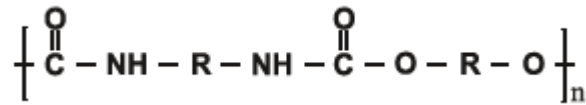


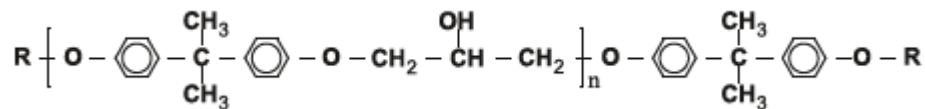
Figure 2.1 Repeating structure examples of thermoplastic polymers; (a) polyethylene and (b) polycarbonate [45]

Figure 2.1 shows examples of unit structure of thermoplastic polymers and Figure 2.2 shows example of unit structure of thermosetting polymers including epoxy resin mentioned in the previous chapter. [45, 55] The difference between those two types is the type of bonding between polymer chains. Thermoplastic chains are bonded with Van der Waals bonds while thermosetting polymers have chemical (covalent) bonds between chains. This difference affects their basic thermal and processing characteristics significantly. Thermoplastic polymers can be melted and molded when

it is heated enough to overcome Van der Waals force between polymer chains. Thermosetting polymers, which are the most commonly used polymeric materials in electronic packaging, solidify by being cured chemically forming cross-links between long chemical chain structures. This cross-linking in a network of molecules prevents thermosetting polymers from melting when they are heated after curing (cross-linking) is done.



(a)



(b)

Figure 2.2 Repeating structure of examples of thermoset polymers; (a) Polyurethane and (b) epoxy based polymers [45]

2.2. Thermomechanical Behavior of Polymers

2.2.1. Cure Shrinkage and Modulus Evolution of Polymeric Materials

During the curing of the thermoset, the single polymer chains form crosslinks between each other. As the result, the bonds between the chains change from van der Waals force to the covalent bonding [56] and the total volume of the structure reduced and the modulus develops during the curing process [57].

Cure shrinkage occurs at the beginning of the curing as the distance between the molecule chains changes during crosslinking and modulus starts to evolve after the gelation point. Since the cure shrinkage with non-zero modulus evolution can be considered as a mechanical strain, residual stresses can be generated during the curing process of polymeric materials. This issue has interested electronic packaging researchers for several years and it has been identified to be important in some cases [58-60].

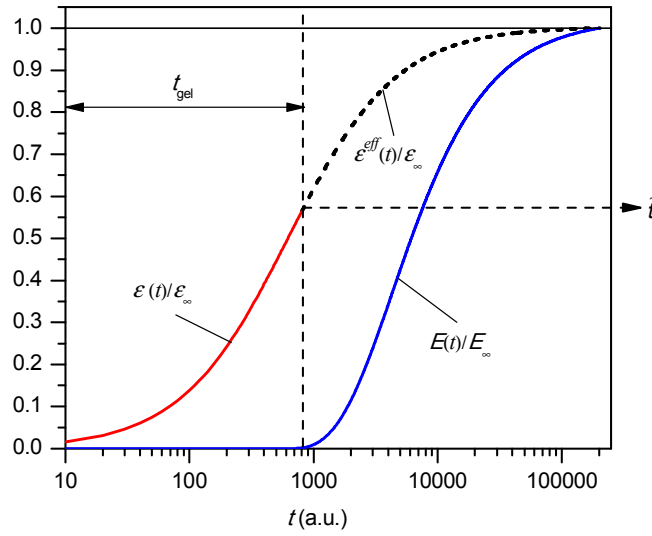


Figure 2.3 Illustration of property evolution in a typical polymer system [61]

The evolution properties of a typical material system are illustrated in Figure 2.3, which defines schematically the cure shrinkage evolution, $\varepsilon(t)$; the effective cure shrinkage evolution, $\varepsilon^{eff}(t)$, defined as the cure shrinkage accumulated after the gelation point t_{gel} , before which the modulus is “zero”; and the modulus evolution, $E(t)$, after the gelation point. For the purpose of illustration, the shrinkage and the modulus are normalized by the total cure shrinkage, ε_{∞} , and the equilibrium modulus, E_{∞} , respectively, and the time axis is shown in an arbitrary unit. Before the gelation

point, no residual stress can be developed because of the zero modulus; after the gelation point, all cure shrinkage contributes to the development of residual stresses [61, 62].

Numerous testing methods have been developed for the measurement of the cure shrinkage. The dilatometer is the most commonly practiced method [20, 63-68], which has been practiced for measuring the shrinkage of different polymeric materials. The advantage of the dilatometer is the direct measurement of the volume change as a function of temperature and pressure. However, the system is relatively complicated, and some the toxic materials are used in the system. A laser scanning micrometer was implemented to monitor the length of a polymer specimen during curing [67]. It only applies to the light curing polymers due to the complex optical setup even though it has high accuracy in the length measurement. A gas pycnometer was used to measure the shrinkage of the dental composites [69]. Due to the lack of the active temperature control system, this system cannot maintain the constant curing temperature. The in-situ monitoring the curing shrinkage was realized by an optical fiber sensor during injection molding [70]. Using the cross section analysis technique, the curing shrinkage of the UV-cured adhesives was measured [71]. The uncertainty in the volume determination could introduce significant error to the results. The cure shrinkage of two epoxy-based NCA materials was studied using a Thermo-mechanical Analyzer (TMA) [72]. However, constant loading was applied to the specimen during curing, which could affect the measured shrinkage. A moiré method was implemented to measure the curing properties of the polymer material with some assumptions [73]. It should be noted that all the methods above only measure the total cure shrinkage,

which includes the shrinkages before the gelation point. Using the total chemical for the prediction would overestimate the warpage and the residual stress because the shrinkage before the gelation point does not have stiffness and thus does not cause stress or warpage [74].

After measuring the total cure shrinkage (or effective cure shrinkage) and equilibrium modulus, the residuals stress and warpage was predicted [20, 22, 26, 63, 64, 75-77]. Only the final value of the shrinkage and modulus were used in these cases. Therefore, only the final warpage is to be predicted. The curing induced strain was assumed to be elastic by curing the polymer above the glass transition temperature [76, 77]. The curing process should also be isothermal in order to eliminate the effect of the thermal expansion. The properties evolution during the curing was not considered in these cases.

The effective cure shrinkage has also been measured by the bi-material strip [75]. By curing the polymer on top of the substrate, the whole assembly will warp only after the polymer layer starts to develop the warpage. By measuring the warpage of the assembly, the effective cure shrinkage can be determined. The gelation point during the curing process can also be determined [72, 78]. For the EMC curing, high pressure and high temperature is needed for the curing requirement, which is not practical to be done by the bi-material strip.

The cure shrinkage and modulus evolution are measured to predict the warpage and the residual stress evolution during the whole curing process [74, 79-81]. It is assumed that the curing process is elastic in these studies. The curing dependent viscoelastic properties were measured for the accurate prediction of the warpage and

residual stress [82-88] evolution during curing. The curing dependent viscoelastic model can be used for the isothermal and non-isothermal curing. The time-temperature-conversion superposition model is applied. It should be noted that the curing-time-temperature dependent properties are very difficult to measure experimentally. The special setup was design to measure the modulus at different curing stages [82, 83, 85]. The time-temperature dependent modulus of the polymer at different curing stages was measured by DMA [87-89].

2.2.2. Coefficient of Thermal Expansion and Glass Transition Temperature

As one of the most important thermo-mechanical properties of polymeric materials, the *coefficient of thermal expansion* (CTE) relates the volume changes that occur in a polymer to the temperature variation. The polymer volume, V , increases with increasing temperature as a result of the increasing atomic motions resulting from the added energy. The *coefficient of volumetric thermal expansion* β is defined as the fractional rate of change of V as a function of temperature T , which can be expressed as

$$\beta(T) = \frac{1}{V(T)} \left[\frac{\partial V(T)}{\partial T} \right]_p \quad (2.1)$$

A partial derivative is used in the above equation because V is also a function of the temperature. The *coefficient of linear thermal expansion*, α is another useful quantity which is more commonly quoted in the literature. It simply equals to one third of the coefficient of volumetric thermal expansion for an isotropic material

$$\alpha = \frac{\beta}{3} \quad (2.2)$$

Unless specifically stated, the CTE in this study means the coefficient of linear thermal expansion, α .

The CTE of a polymeric material changes dramatically when temperature is at a certain value. This particular temperature is called *glass transition temperature* (T_g). The glass transition temperature is the temperature of amorphous polymers at which increased molecular mobility results in significant changes in their thermomechanical properties [90]. The CTE of a polymer increases dramatically when temperature increases beyond T_g (in the rubbery state). The phenomenon can be explained by the free volume theory. Generally, the volume of a material, V , is the sum of the volume occupied by the molecules, V_0 , and the free volume, V_f , which is the space not occupied by molecules [91]. The free volume is sensitive to changes in temperature and the thermal expansion of polymers can be attributed to a change in free volume. When the temperature decreases from high to low, the free volume shrinks until it is too small to allow long-range cooperative motions, and the temperature at this point is T_g . Below T_g only local conformational changes are permitted and consequently the free volume shows negligible temperature dependence.

In electronic packaging, characterization of the CTE of a polymeric material is critical as it is required for the assessment of the reliability of a packaging product under thermal loadings. Different components in a package have different CTE values. For example, a silicon chip has a CTE of 2.5 ppm/°C; copper pad has a CTE of 17 ppm/°C; a ceramic substrate has a CTE ranging from 4 to 10 ppm/°C while an organic substrate has a CTE ranging from 18 to 24 ppm/°C; the solder material has a CTE ranging from 22 to 26 ppm/°C [1]. The CTE mismatch among different components

produce stresses when subjected to temperature excursions. In design considerations, polymers such as underfills and EMC with appropriate CTE and T_g should be used for optimum stress management.

Thermo-mechanical Analyzer (TMA) is the most widely used tool to measure CTE [ASTM E831]. It is a quartz dilatometer, which consists of a stage which supports the specimen and a quartz probe that moves vertically. The quartz probe is essentially a displacement sensor and a small force of 1 to 100 mN is applied to keep the probe in contact with the specimen. The temperature of the specimen is controlled by the oven. The CTE of the specimen can be calculated by

$$\alpha = \frac{1}{L_0} \frac{\Delta L}{\Delta T} \quad (2.3)$$

where L_0 is the initial height of the specimen, ΔL is the change in height due to a temperature change ΔT .

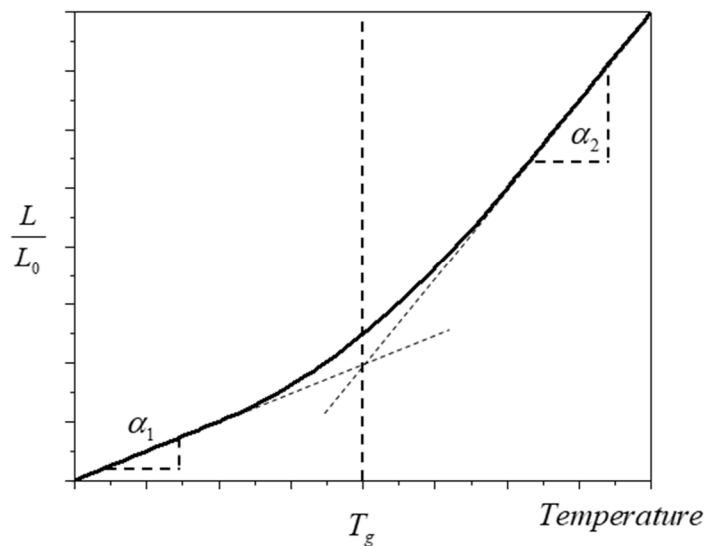


Figure 2.4 Illustration of CTE and T_g measurement using TMA

TMA can be also employed to determine T_g . As previously discussed, the CTE of a polymeric material undergoes a dramatic and discontinuous change at T_g . Using the measured displacement-temperature curve, T_g is determined at the inflection point as illustrated in Figure 2.4 where α_1 and α_2 are the CTE below and above T_g , respectively.

T_g can be determined using other properties that change considerably at T_g such as specific heat, refractive index, and dielectric constant. Based on that, DSC, a refractometry, or a dielectric relaxation spectroscopy can be used to detect T_g which essentially measures specific heat, the refractive index, or the dielectric constant of a material, respectively [92].

2.2.3. Viscoelasticity of Polymers

When a strain is applied to the cured thermosetting polymer, the polymer molecule, which is composed of chain and bonds between chains, can be re-arranged depending on its molecular mobility. This rearrangement of molecules causes the time-dependent behavior of these materials. Polymer materials also can respond to the applied stress by stretching its chemical bond in the molecule, which is instantaneous and reversible. The mobility of the molecular arrangement is influenced by many physical and chemical factors, and one of the important factors is temperature. This mobility, which is the rate of the molecular arrangement, is often described with the Arrhenius relation as shown below and in Figure 2.5.

$$\text{rate} \propto \exp\left(\frac{-E}{RT}\right) \quad (2.4)$$

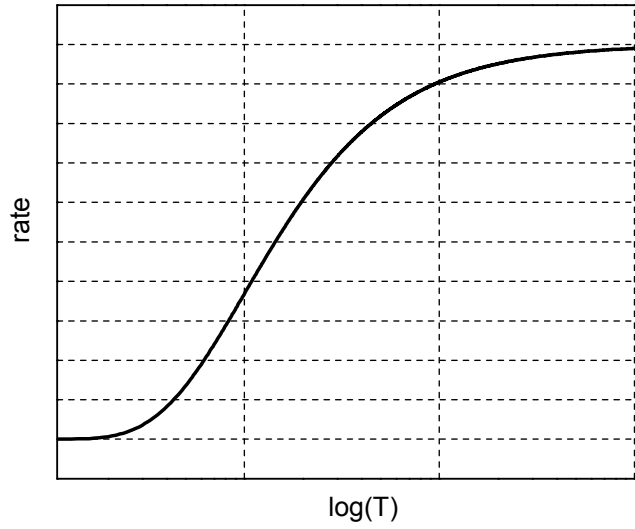


Figure 2.5 Arrhenius relationship

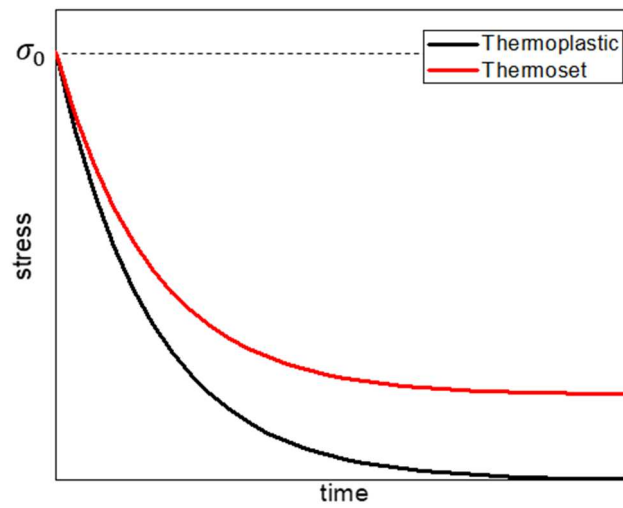
At low temperatures, the rate is very low since this uncoiling re-arrangement process is essentially frozen, and the polymer is able to respond only by the stretching of the chemical bonds. Polymers in this state respond in a “glassy” manner, where the response is instantaneous and brittle. Conversely, when the rate is very high, the re-arrangement happens very fast, practically instantaneously. At this state, the polymer exhibits instantaneous and fully reversible large strain and respond in a “rubbery” manner. With the nature of the Arrhenius relationship, the re-arranging rate dramatically increase at a certain temperature, which is the glass transition temperature of the polymer. Significant time-dependent behavior is observed in this region, and it is called “leathery” or “viscoelastic” behavior [32].

Creep and stress relaxation tests are used to characterize the viscoelastic behavior. In a relaxation test, a constant strain is applied and maintained during the duration of the test. When the constant strain is applied, the stress needed to maintain

the constant strain will decrease with time. Decreasing stress eventually approaches zero for an ideal thermoplastic polymer and a certain constant value for a thermosetting polymer. Figure 2.6 describes the strain input and stress output of the stress relaxation test on ideal thermoplastic and thermoset materials [45].



(a)



(b)

Figure 2.6 Stress relaxation test: (a) strain input and (b) stress output

The ratio between the time dependent stress and applied stress defines relaxation modulus, which can be expressed as

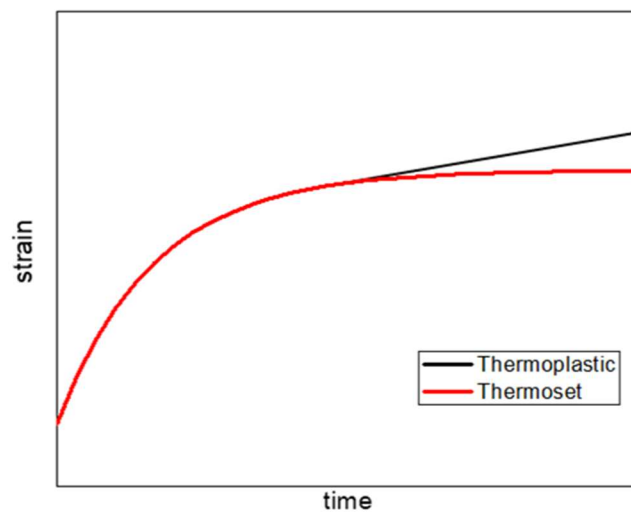
$$E(t) = \frac{\sigma(t)}{\varepsilon_0} \quad (2.5)$$

where $E(t)$ is relaxation modulus, ε_0 is applied strain during the stress relaxation test.

It should be noted that equation (2.5) is only valid when a constant strain is applied and cannot be substituted with $\varepsilon(t)$ when time dependent strain is applied to the material.



(a)



(b)

Figure 2.7 Creep test: (a) stress input and (b) strain output

For a thermosetting material, the limiting moduli at $t = 0$ and $t = \infty$ is called initial modulus and equilibrium modulus, respectively.

In a creep test, a constant stress is applied to the material. In this case, strain under the constant load increases with time, and this test defines creep compliance which can be expressed as

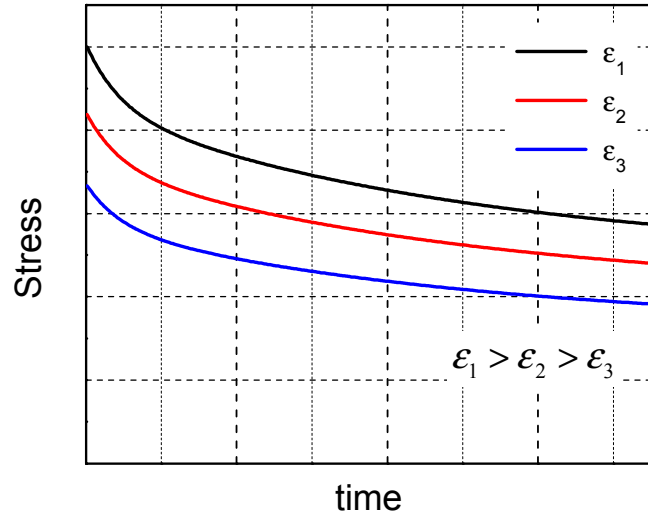
$$D(t) = \frac{\varepsilon(t)}{\sigma_0} \quad (2.6)$$

where $D(t)$ is creep compliance, σ_0 is applied stress and $\varepsilon(t)$ is the time dependent strain observed during the creep test. In a creep test, the strain will increase without bound over time for a thermoplastic polymer while the strain will approach a constant value after a long time for a thermosetting polymer, as schematically illustrated in Figure 2.7. As shown in Figure 2.7, a strain rate under the constant stress becomes constant after a sufficiently long period of time. This fluid-like characteristic of thermoplastic polymers is due to lack of primary (covalent) bonds between molecular chains while thermosetting polymers which has crosslinks, covalent bonds between molecular chains has solid characteristics.

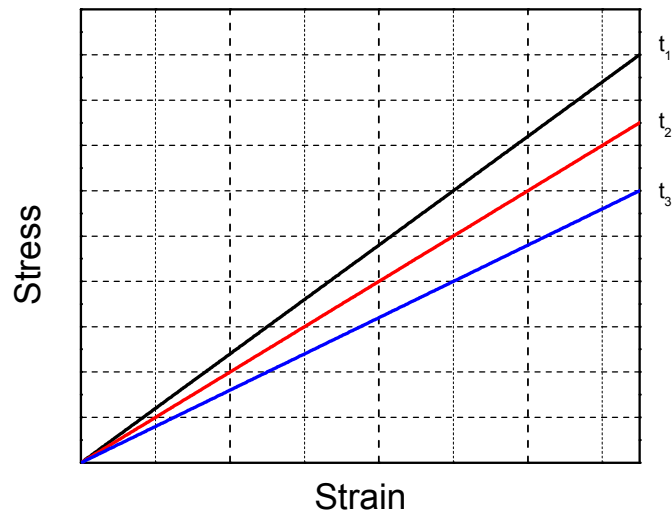
2.2.4. Linear Viscoelasticity and Boltzmann Superposition Principle (BSP)

For many applications and analysis, it is important to determine if the viscoelastic behavior of the polymer is linear or not. Linear viscoelasticity requires both superposition and proportionality for its response at given time, which implies that the time dependent behavior is independent to applied stress or strain. Linearity of the viscoelastic material can be shown by isochronous stress-strain relationship from stress

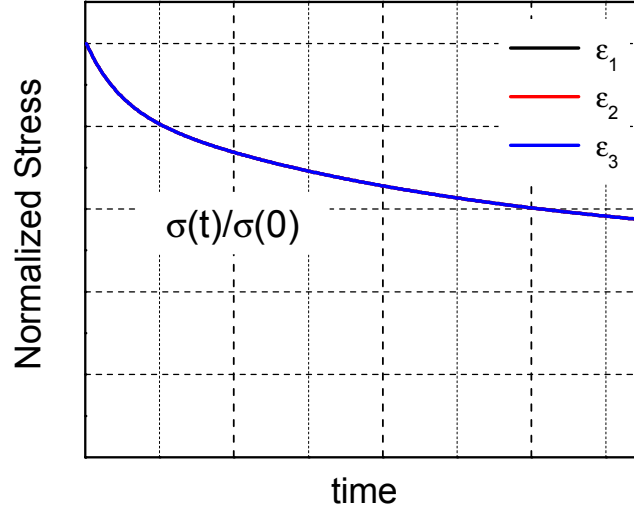
relaxation (or creep) test with different loading levels. Isochronous stress and strain data from independent stress relaxation or creep test are linearly proportional to each other if the linear viscoelasticity is valid for the material [45].



(a)



(b)



(c)

Figure 2.8 (a) Stress relaxation test, (b) isochronous stress-strain relationship, and (c) normalized stress of stress relaxation test results of material with linear viscoelastic behavior

Figure 2.8(a) shows the stress relaxation test of a linear viscoelastic material at three different strain levels. If the stress and 3 different strain values at a given time is plotted, three points will fall onto a straight line depending on the given time, as shown in Figure 2.8(b). The slope of isochronous stress-strain relationship is higher for t_1 because the modulus of the material relaxes over time. The normalized stress curves, i.e., the curve of stress values over time divided by the initial stress value from stress relaxation test of linear viscoelastic material, are identical to each other.

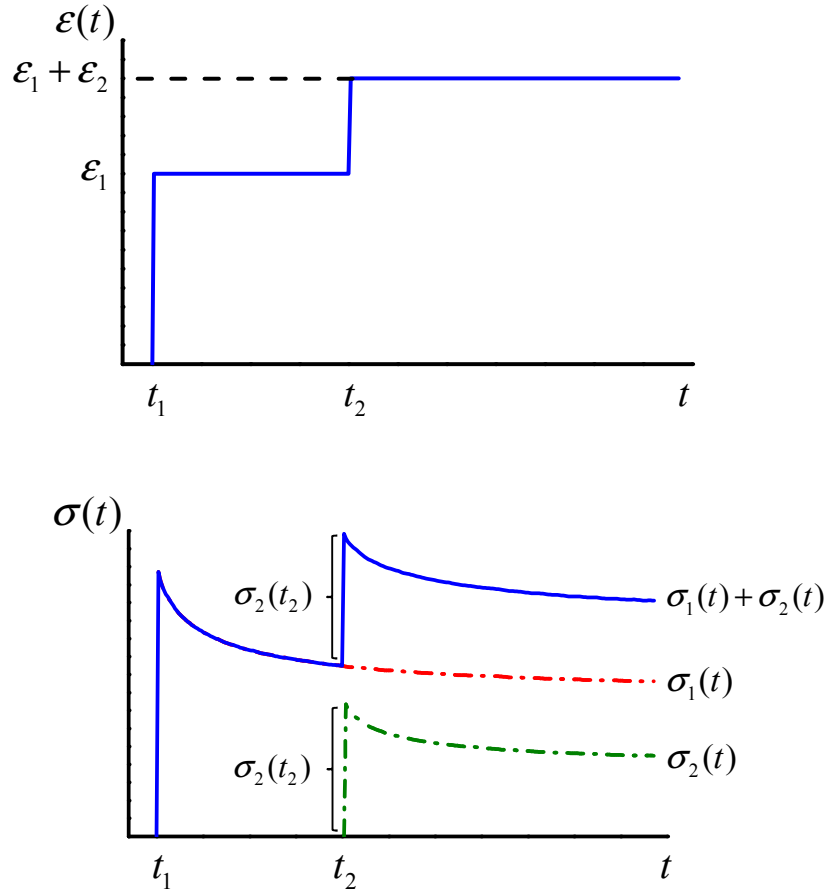


Figure 2.9 Boltzmann superposition principle example

This linearity of the viscoelastic material enables to describe the behavior of the material using a time dependent constitutive equation, which is not a function of applied loading condition for general loadings using Boltzmann superposition principle (BSP). The Boltzmann superposition principle states that “in the linear viscoelastic regime the strain response to successive stress are additive” [45]. Therefore, when time dependent Young’s modulus of a linear viscoelastic material is known, the stress of the material for discretely applied separate uniaxial strain, $\Delta\epsilon_n$, at time, τ_n can be described as:

$$\sigma(t) = E(t)\epsilon_0 + E(t-\tau_1)\cdot\Delta\epsilon_1 + E(t-\tau_2)\cdot\Delta\epsilon_2 + E(t-\tau_3)\cdot\Delta\epsilon_3 + \dots \quad (2.7)$$

An example is shown in Figure 2.9, where the stress is shown as a function of time when two different strains ε_1 and ε_2 are applied at t_1 and t_2 , respectively. The stress can be expressed as:

$$\sigma(t) = \sigma_1(t) + \sigma_2(t) = E(t-t_1)\Delta\varepsilon_1 + E(t-t_2)\Delta\varepsilon_2 \quad (2.8)$$

For general loading condition, the BSP can be described as

$$\sigma(t) = \int_{-\infty}^t E(t-\tau) \frac{d\varepsilon(\tau)}{d\tau} d\tau \quad (2.9)$$

It also can be written for compliance as

$$\varepsilon(t) = \int_{-\infty}^t D(t-\tau) \frac{d\sigma(\tau)}{d\tau} d\tau \quad (2.10)$$

Therefore, for a homogeneous isotropic material, behavior of linear viscoelastic material can be described using the following constitutive equations. [93]

$$\begin{aligned} s_{ij}(t) &= 2 \int G(t-\tau) \frac{\partial e_{ij}(\tau)}{\partial \tau} d\tau \\ \sigma_{kk}(t) &= 3 \int K(t-\tau) \frac{\partial \varepsilon_{kk}(\tau)}{\partial \tau} d\tau \end{aligned} \quad (2.11)$$

where s_{ij} and σ_{kk} are deviatoric and hydrostatic stress components, e_{ij} and ε_{kk} are deviatoric and hydrostatic strain constant, G and K are time dependent shear and bulk modulus.

In addition, these two equations (2.9) and (2.10) can be used to show the relationship between time dependent modulus and compliance. Taking the Laplace transform of these two equations yields

$$\bar{\sigma}(s) = s\bar{E}(s)\bar{\varepsilon}(s) \quad (2.12)$$

$$\bar{\varepsilon}(s) = s\bar{D}(s)\bar{\sigma}(s) \quad (2.13)$$

Combining these two equations yields

$$\frac{1}{s^2} = \bar{E}(s)\bar{D}(s) \quad (2.14)$$

Inverse Laplace transform of equation (2.14) yields

$$t = \int_0^t E(t-\tau) D(\tau) d\tau \quad (2.15)$$

This enables interchange between “relaxation modulus” which can be obtained from stress relaxation test and “compliance” from creep test when those moduli are independent of applied loading, i.e., the material shows linear viscoelasticity.

2.2.5. Thermorheologically Simple (TRS) and Time-Temperature Superposition

As mentioned earlier, the relaxation rate is proportional to the temperature. Thermorheologically simple (TRS) assumption states that all relaxation times of the polymer must be affected by temperature in the same way, and therefore the shapes of the master curve of time dependent moduli of the polymer are the same in the log time scale at different temperatures. This assumption is not always valid to all the polymeric materials but has been found to hold for a various array of homogeneous polymer systems [2, 46-50]. This enables using time dependent modulus obtained in a temperature can be used to analyze the behavior of the polymer in other temperatures.

The relaxation time of the polymer at one temperature can be found from the relaxation time at the reference temperature and the shift factor between the temperature and the reference temperature. This can be expressed mathematically using the shift factor a_T as:

$$\tau(T) = a_T \tau(T_{ref}) \quad (2.16)$$

where τ is temperature dependent relaxation time of the polymer, T_{ref} is the reference temperature from which the shift factor is defined. Because it is multiplication of the time, the shift factor defines the amount of the shift of the modulus curve in a log time scale

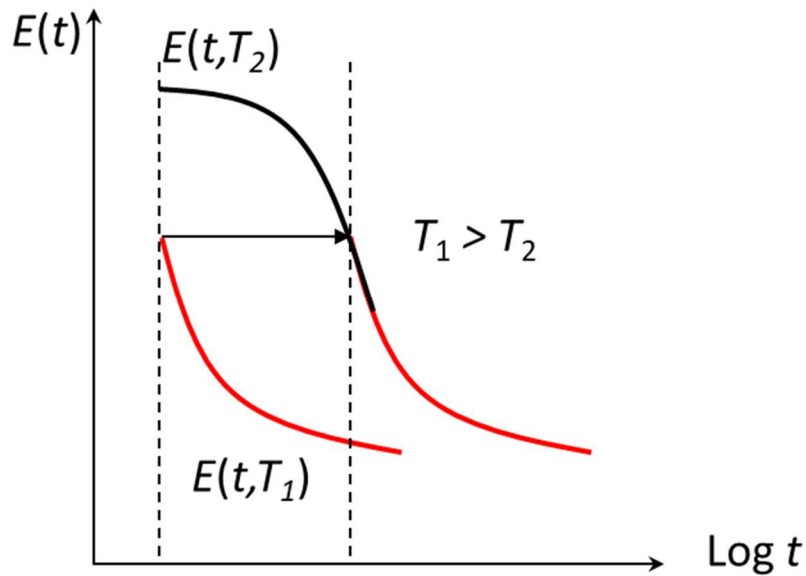


Figure 2.10 Description of time-temperature superposition

The TRS assumption also enables time-temperature superposition. It is practically impossible to obtain a complete time dependent modulus master curve at one temperature. Relaxation behavior takes too long at low temperature to record completely, or too fast at high temperature to capture the glassy behavior at early stages. However, the master curve can be obtained by shifting the modulus curves obtained from various temperatures and shift them on the log time scale, as illustrated in Figure 2.10. In Figure 2.10, the time dependent Young's modulus is obtained in two different temperatures. The modulus measured in T_1 which is higher than T_2 can be shifted in the log time scale while it is maintaining the shape of the curve in the log time scale

when TRS is valid. When two curves are overlapped as shown in the figure, it can be considered as extended Young's modulus at T_2 . The amount of shift used to construct the master curve is the shift factor of the temperature where the specific segment of master curve is obtained.

2.3. Fiber Bragg Grating as a Sensor

The Fiber Bragg Grating (FBG) has been used as a sensor for strain measurement for various materials, most notably composite materials [4, 51-59]. The FBG was embedded in the structure to measure strain caused by thermal expansion [51, 52, 57], moisture absorption [54, 55, 60] and curing [56, 58, 59].

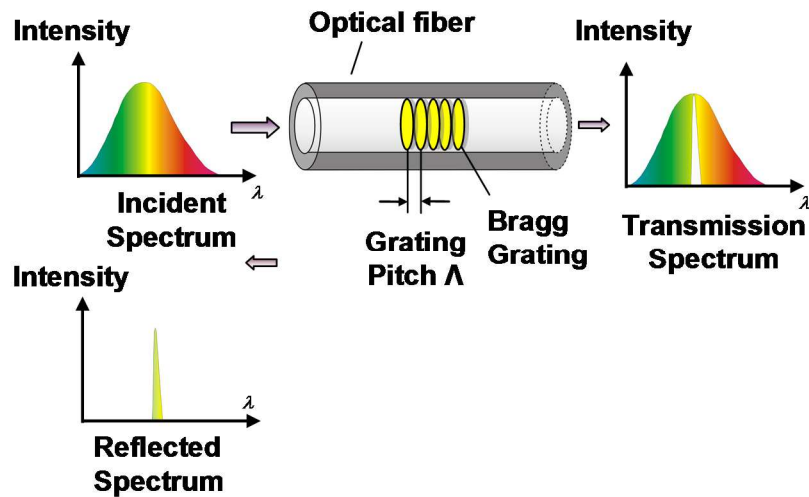


Figure 2.11 Illustration of an FBG spectrum reflection and transition [4]

A fiber Bragg grating is formed by a periodic perturbation of refractive index along the fiber length, which is typically created by the exposure to the intense interference pattern of UV energy [61-63]. When a band of the incident light encounters a material of higher index refraction, some of the incident light is reflected and some is transmitted. As shown in Figure 2.11, only small portion of the incident

light can be reflected and the peak of the reflected light is called the Bragg wavelength which should satisfies [61-63]

$$\lambda = 2n_{eff}\Lambda \quad (2.17)$$

where λ is the Bragg wavelength, n_{eff} is the effective refractive index and Λ is the grating pitch. Each grating serves to reflect a portion of the light signal and the total amount of the light reflected is dependent on the perturbed refractive index and the total grating length.

The grating pitch Λ and the effective refractive index n_{eff} can be changed due to the external disturbances such as the strain and temperature, resulting in the shifting of the Bragg wavelength. This is the basic principle of using FBGs as a sensor or temperature sensor.

The Equation (2.17) can be differentiated into,

$$\frac{\Delta\lambda}{\lambda} = \frac{\Delta\Lambda}{\Lambda} + \frac{\Delta n_{eff}}{n_{eff}} = \epsilon_1 + \frac{\Delta n_{eff}}{n_{eff}} \quad (2.18)$$

where $\Delta\Lambda$ and Δn_{eff} are the changes in the grating pitch and the effective refractive index respectively, and ϵ_1 is the axial strain along the fiber. For the isotropic and straight Bragg grating, the effective refractive index change can be expressed as[64],

$$\Delta n_{eff} = -\frac{n^3}{2} \left[P_{12}\epsilon_1 + (P_{11} + P_{12})\epsilon_2 - \left\{ \frac{2}{n^3} \frac{dn}{dT} + (P_{11} + 2P_{12})\alpha_f \right\} \Delta T \right] \quad (2.19)$$

where ϵ_2 is the transverse strain, P_{ij} are strain-optical coefficients (Prockel's coefficients), $\frac{dn}{dT}$ is the thermal-optical coefficient, α_f is the CTE of the fiber core

material, and ΔT is the temperature change. For the uniaxial loading where $\varepsilon_2 = -\nu\varepsilon_1$ with no temperature change, Equations (2.18) and (2.19) can be simplified as

$$\Delta\lambda = \lambda(1 - P_k)\varepsilon_1 \quad (2.20)$$

where P_k is defined as $P_k = -\frac{n^2}{2}[P_{12} - \nu(P_{11} + P_{12})]$, ν is the Poisson's ratio of the fiber material. Equation (2.20) shows the linear relationship between the applied strain and the BW change.

When both temperature and mechanical loading are incorporated in the grating, the total BW shift can be expressed as:

$$\Delta\lambda = \Delta\lambda_t + \Delta\lambda_d \quad (2.21)$$

where $\Delta\lambda_t$ is the BW change by the temperature; $\Delta\lambda_d$ is the BW change caused by the mechanical loading. They can be expressed as[65, 66]:

$$\Delta\lambda_t = \lambda_d \left[\left(\alpha_f + \frac{1}{n_{eff}} \frac{dn}{dT} \right) \Delta T + \frac{1}{n_{eff}} \frac{dn}{dT} \cdot \alpha_f \Delta T^2 \right] \quad (2.22)$$

$$\Delta\lambda_d = \frac{1}{E_f} \left\{ \begin{array}{l} \left[1 - \frac{n^2}{2} (P_{12} - (P_{12} + P_{11})\nu_f) \right] \sigma_{zz}^f \\ - \left[2\nu_f + \frac{n^2}{2} ((1 - \nu_f)P_{11} + (1 - 3\nu_f)P_{12}) \right] \sigma_{rr}^f \end{array} \right\} \lambda \quad (2.23)$$

Depends on the application, these governing equations can be utilized to conduct measurement using FBG. When FBG is embedded in a structure where the volume stiffness of the fiber is negligible, the documented BW change and the governing equation can be used to monitor structure's strain caused by thermal expansion, moisture absorption, and etc. Also, they can be used to inversely calculate

material properties when the fiber with FBG is embedded in a specimen of the target material based on the analytical relationship between the material properties of the specimen and the deformation of the fiber.

Chapter 3 Time dependent Property Measurements by FBG

Embedded Specimen

The method to measure two time-dependent elastic constants is described. An FBG sensor is embedded in a cylindrical specimen, and the constants are calculated from governing equations that provide relationships between BW changes and properties. The specimen configuration is described first with governing equations, and a detailed measurement procedure is followed.

3.1. Specimen Configuration and Governing Equations

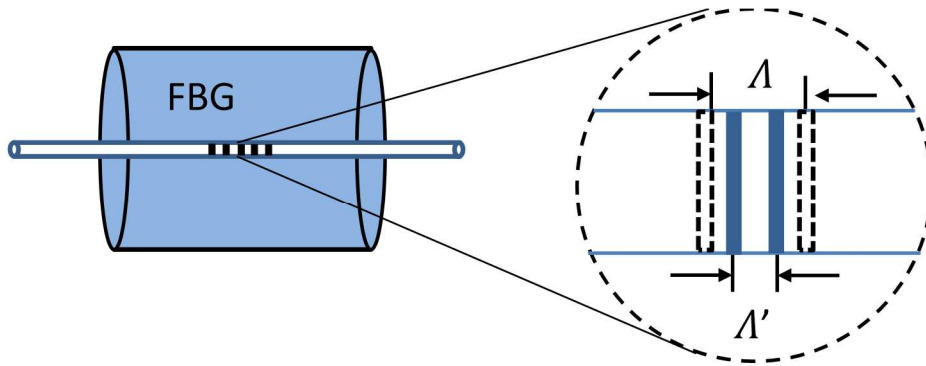


Figure 3.1 FBG embedded in the Cylindrical Specimen

An FBG is embedded in a cylindrically shaped specimen, as shown in Figure 3.1. The optical fiber containing the FBG is placed along the axial direction of the cylinder. As mechanical loading is applied to the specimen, Bragg wavelength of the grating embedded in the specimen will change as the fiber deforms together with the specimen. Then the time dependent moduli can be inversely calculated using equation (2.23) once analytical relationship between the properties of the specimen, applied load, and the stresses within the fiber is developed.

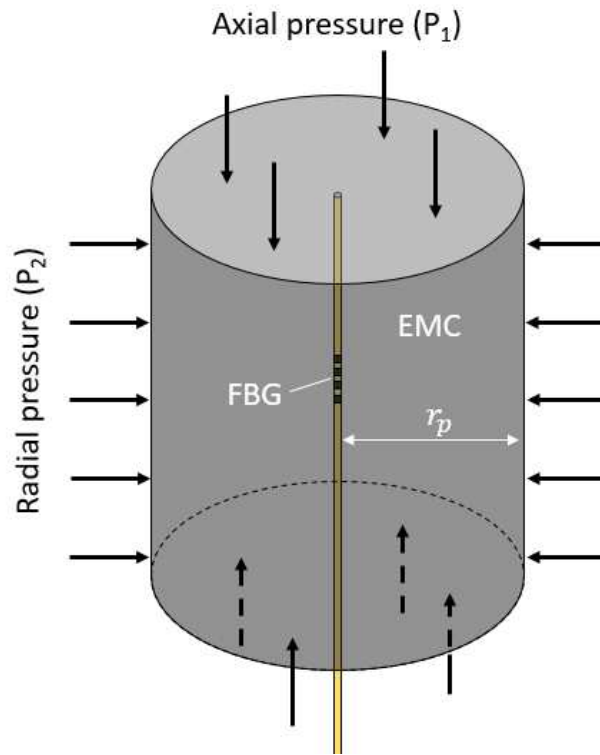


Figure 3.2 Schematic of a polymer specimen with embedded FBG under axial and radial loading

When the axial stress P_1 and radial stress P_2 is applied to the cylindrical specimen as shown in Figure 3.2, stress components of the fiber can be expressed as following from the generalized plane strain solution. [1-3]:

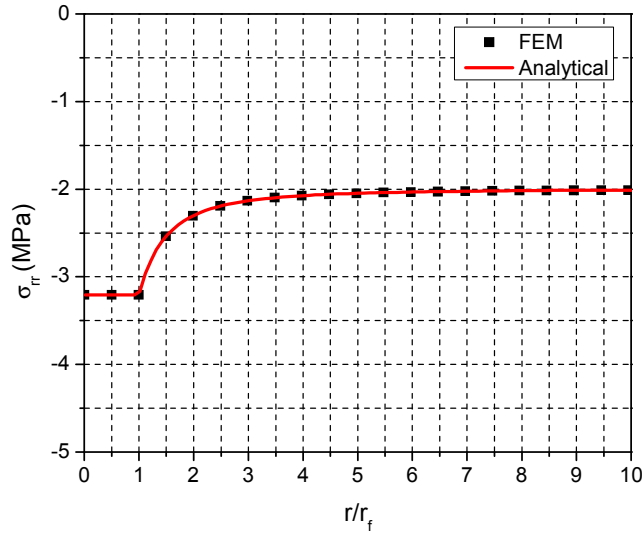
$$\begin{aligned}
\sigma_{zz}(r) &= \frac{2E_f}{1+\nu_f} \frac{C_{1f}}{1-2\nu_f} + \frac{2E_f\nu_f^2c}{(1+\nu_f)(1-2\nu_f)} + E_fc, \quad 0 \leq r \leq r_f \\
\sigma_{rr}(r) &= \frac{E_f}{1+\nu_f} \left[\frac{C_{1f}}{1-2\nu_f} - \frac{C_{2f}}{r^2} \right] + \frac{E_f\nu_fc}{(1+\nu_f)(1-2\nu_f)}, \quad 0 \leq r \leq r_f \\
\sigma_{\theta\theta}(r) &= \frac{E_f}{1+\nu_f} \left[\frac{C_{1f}}{1-2\nu_f} + \frac{C_{2f}}{r^2} \right] + \frac{E_f\nu_fc}{(1+\nu_f)(1-2\nu_f)}, \quad 0 \leq r < r_f \\
\sigma_{zz}(r) &= \frac{2E_p}{1+\nu_p} \frac{C_{1p}}{1-2\nu_p} + \frac{2E_p\nu_p^2c}{(1+\nu_p)(1-2\nu_p)} + E_pc, \quad r_f \leq r \leq r_p \\
\sigma_{rr}(r) &= \frac{E_p}{1+\nu_p} \left[\frac{C_{1p}}{1-2\nu_p} - \frac{C_{2p}}{r^2} \right] + \frac{E_p\nu_pc}{(1+\nu_p)(1-2\nu_p)}, \quad r_f \leq r \leq r_p \\
\sigma_{\theta\theta}(r) &= \frac{E_p}{1+\nu_p} \left[\frac{C_{1p}}{1-2\nu_p} + \frac{C_{2p}}{r^2} \right] + \frac{E_p\nu_pc}{(1+\nu_p)(1-2\nu_p)}, \quad r_f < r \leq r_p
\end{aligned} \tag{3.1}$$

where r_f, r_p are the radius of the fiber and polymer specimen respectively, $\sigma_{zz}^f, \sigma_{rr}^f$ and $\sigma_{\theta\theta}^f$ are the axial, radial and hoop stress components of the fiber, respectively, E_p, ν_p are the modulus and Poisson's ratio of the polymer specimen, and

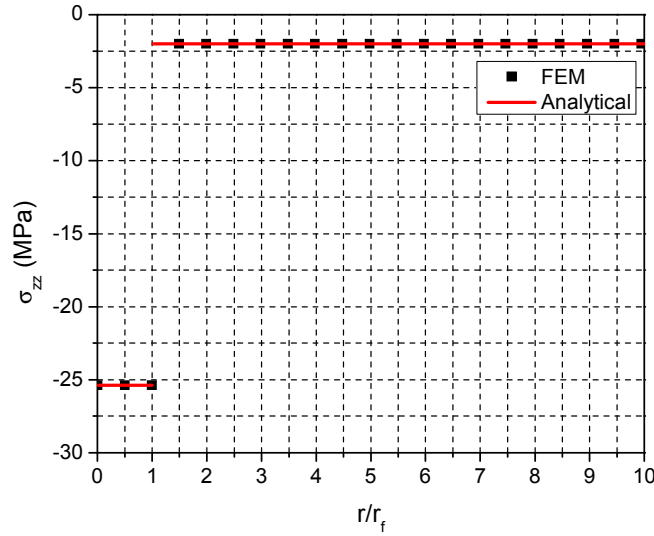
$$\begin{aligned}
C_{1p} &= \frac{CE - BF}{AE - BD} \\
C_0 &= \frac{CD - AF}{BD - AE} \\
C_{2p} &= \left(\frac{C_{1p}}{(1-2\nu_p)(1+\nu_p)} + \frac{\nu_p C_0}{(1-2\nu_p)(1+\nu_p)} - \frac{P_1}{E_p} \right) (1+\nu_p)r_p^2 \\
C_{1f} &= C_{1p} + \frac{C_{2p}}{r_p^2} \\
C_{2f} &= 0
\end{aligned} \tag{3.2}$$

$$\begin{aligned}
A &= \frac{E_p}{(1+\nu_p)(1-2\nu_p)} \left(\frac{r_p^2}{r_f^2} - 1 \right) + \frac{E_f}{(1+\nu_f)(1-2\nu_f)} \left(1 + \frac{r_p^2}{r_f^2(1-2\nu_p)} \right) \\
B &= \frac{E_p \nu_p}{(1+\nu_p)(1-2\nu_p)} \left(\frac{r_p^2}{r_f^2} - 1 \right) + \frac{E_f \nu_f}{(1+\nu_f)(1-2\nu_f)} \left(1 + \frac{r_p^2}{r_f^2(1-2\nu_p)} \frac{\nu_p}{\nu_f} \right) \\
C &= \left(1 + \frac{E_f}{(1+\nu_f)(1-2\nu_f)} \frac{(1+\nu_p)}{E_p} \right) \frac{r_p^2}{r_f^2} P_2 \\
D &= \frac{2E_p \nu_p}{(1+\nu_p)(1-2\nu_p)} \left(\frac{r_p^2}{r_f^2} - 1 \right) + \frac{2E_f \nu_f}{(1+\nu_f)(1-2\nu_f)} \left(1 + \frac{r_p^2}{r_f^2(1-2\nu_p)} \right) \\
E &= \frac{2E_p \nu_p}{(1+\nu_p)(1-2\nu_p)} \left(\frac{r_p^2}{r_f^2} - 1 \right) + \frac{2E_f \nu_f}{(1+\nu_f)(1-2\nu_f)} \left(\nu_f + \frac{\nu_p r_p^2}{r_f^2(1-2\nu_p)} \right) \\
&\quad + E_f + E_p \left(\frac{r_p^2}{r_f^2} - 1 \right) \\
F &= \frac{2E_f \nu_f}{(1+\nu_f)(1-2\nu_f) E_p} (1+\nu_p) \frac{r_p^2}{r_f^2} P_2 + \frac{r_p^2}{r_f^2} P_1
\end{aligned} \tag{3.3}$$

The solution is verified by comparing with the FEM result of the stress within the FBG embedded specimen under hydrostatic stress as shown in Figure 3.3.



(a)



(b)

Figure 3.3 Analytical solution verification for σ_{rr} and σ_{zz} within a FBG embedded specimen

Analytical solution shown in chapter 3.1 shows that the Bragg wavelength can be expressed a function of Young's modulus and the Poisson's ratio of the polymer specimen for the given specimen configuration $\beta = \frac{r_p}{r_f}$ and loading condition as shown below.

$$\Delta\lambda_B = \Pi(E_p, \nu_p, P_1, P_2, \beta) \quad (3.4)$$

where $\Delta\lambda_B$ is Bragg wavelength change upon loading, E_p is Young's modulus of polymer, ν_p is Poisson's ratio of polymer, P_1 and P_2 is axial and radial loading to the specimen, respectively. When a set of data is obtained from a test the loading condition (P_1 and P_2) and the specimen configuration are known, and the Bragg wavelength change is the measured quantity from the experiment. The constants are calculated

from governing equations that provide relationships between BW changes and properties.

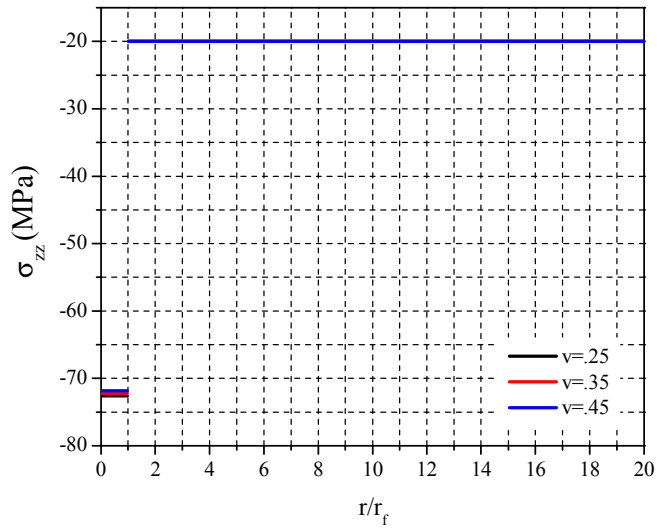
3.2. Sequential Iterative Procedure to Obtain Two Constants

There are two unknowns (E_p, ν_p) in the governing equations. Theoretically, two data sets of $\Delta\lambda_B$ obtained from two different loading conditions, e.g., uniaxial ($P_1 = p$ and $P_2 = 0$) and hydrostatic ($P_1 = P_2 = p$), can be utilized to determine the two constants through a non-linear regression analysis.

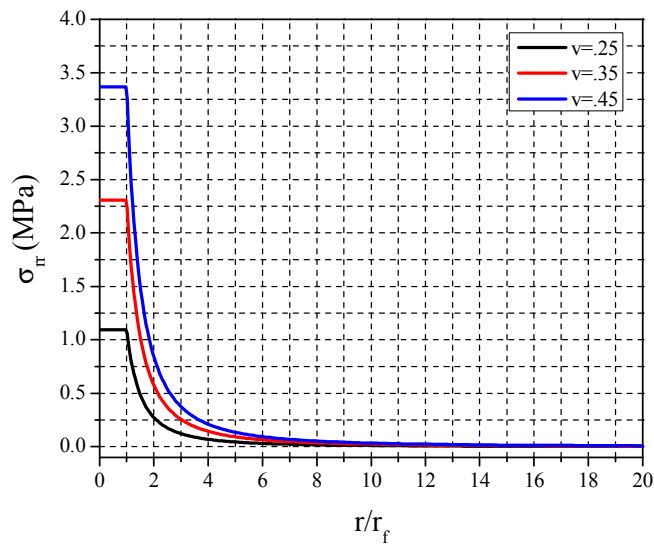
The governing equations are extremely non-linear in nature, and it would be difficult to obtain a unique set of E_p and ν_p , especially when experimental data contain some uncertainties; i.e., the convergence after the non-linear regression may not necessary guarantee a correct set of E_p and ν_p . This problem can be exacerbated when the properties are to be determined as a function time. A sequential iterative procedure is proposed to cope with the problem, where the simple nature of the uniaxial loading is exploited.

The uniaxial tension produces a single stress field, and thus Young's modulus is readily measured by documenting a strain in the loading direction. The FBG embedded specimen is a composite structure, and the radial stresses (σ_{rr}) is zero only when ν_p is identical to ν_f .

Figure 3.4 shows the distributions of σ_{zz} and σ_{rr} for three different values of ν_p when a specimen ($\beta = 100$ and $E_p = 20$ GPa) is subjected to a uniaxial loading of 20 MPa in compression.



(a)



(b)

Figure 3.4 stress (a) σ_{zz} and (b) σ_{rr} of the FBG when a specimen is subjected to a uniaxial compression loading

It is worth noting that the axial stress of the polymer (σ_{zz}^p) is the same as the applied stress as expected, while the axial stress (σ_{zz}^f) of the FBG is much higher. It is attributed to the fact that the much smaller E_p and thus much larger polymer axial strain is transferred to the FBG.

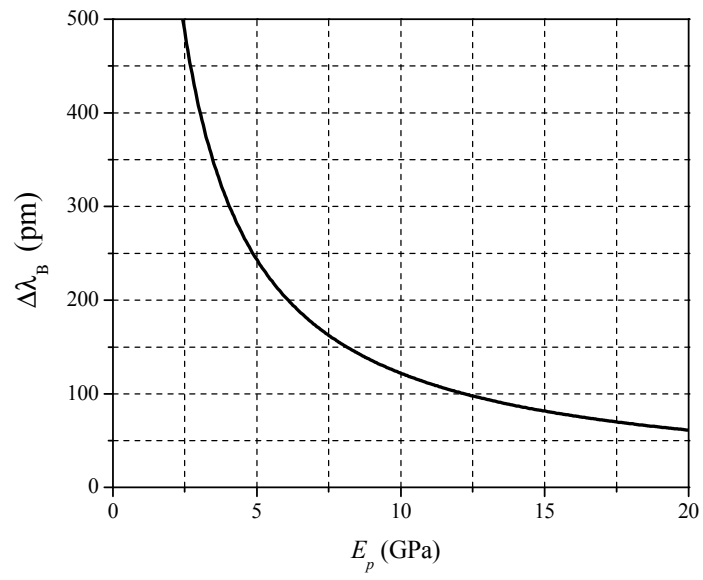
As expected, the radial stress (σ_{rr}) is finite and nearly constant within the FBG, and rapidly decreases to zero. It is important to note that its magnitude within the fiber is an order of magnitude smaller than σ_{zz}^f although it varies with the Poisson's ratio difference between the fiber and the polymer.

Recall the relationship between the BW change and the stresses of FBG

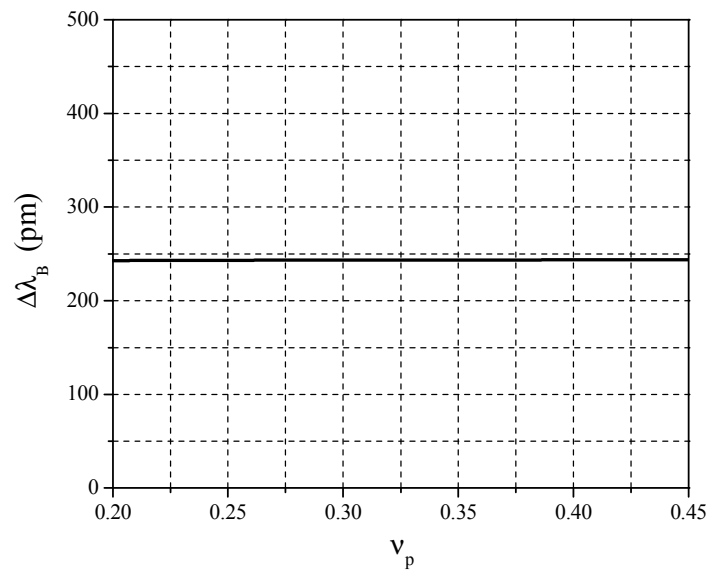
$$\Delta\lambda_B = \frac{\lambda_0}{E_f} (0.784\sigma_{zz}^f - 0.587\sigma_{rr}^f) \quad (3.5)$$

where $\sigma_{zz,f}$ and $\sigma_{rr,f}$ are the axial stress and radial stress of the fiber, respectively. It is clear from the above equation that the effect of ν_p on the BW change would be minimal compared to the effect of E_p .

This is illustrated in Figure 3.5, where the BW changes under uniaxial stress of 1 MPa are plotted as a function (a) E_p and (b) ν_p . The results confirm that E_p affects the BW much more significantly than ν_p . This implies that E_p can be calculated with reasonable accuracy even when ν_p is not correct. This provides a technical rationale for the proposed sequential iterative procedure.



(a)



(b)

Figure 3.5 BW change under uniaxial loading as a function of (a) E_p and (b) ν_p

In the proposed procedure, E_p is first estimated from the BW shift obtained from the uniaxial loading using a representative value of ν_f , e.g., 0.25. Then, the estimated E_p is used to determine ν_p from the BW shift obtained from the hydrostatic loading. Then, the calculated ν_p is used to recalculate E_p from the uniaxial test data. The process is repeated until the values converge. This procedure will ensure a proper set of E_p and ν_p , especially when they change rapidly as a function time, e.g., near T_g .

The existing data is utilized to illustrate the procedure. A set of time-dependent E_p and ν_p available in the literature is shown in Figure 3.6. The corresponding BW shifts obtained from the uniaxial loading and the hydrostatic loading using the governing equations are shown in Figure 3.7.

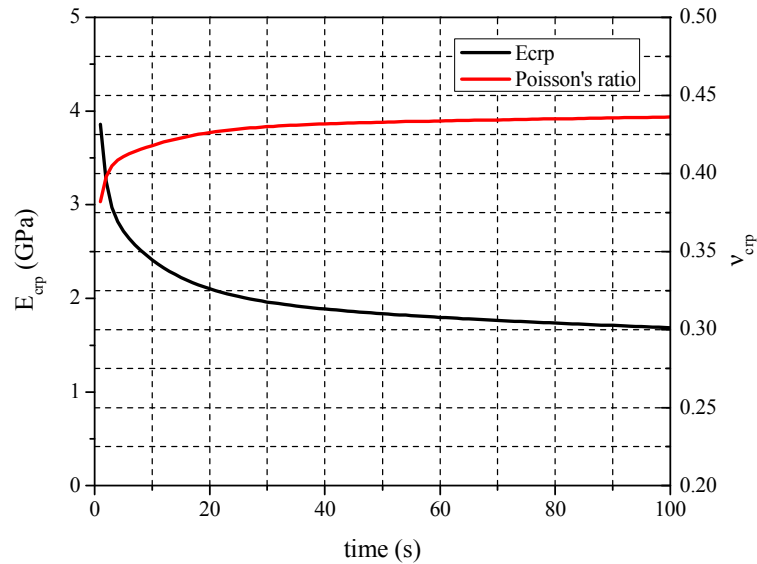


Figure 3.6 Example Young's modulus and Poisson's ratio

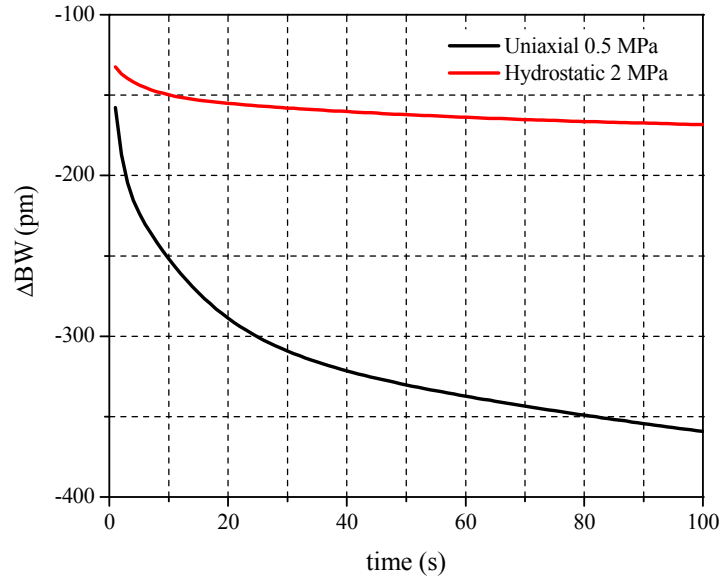
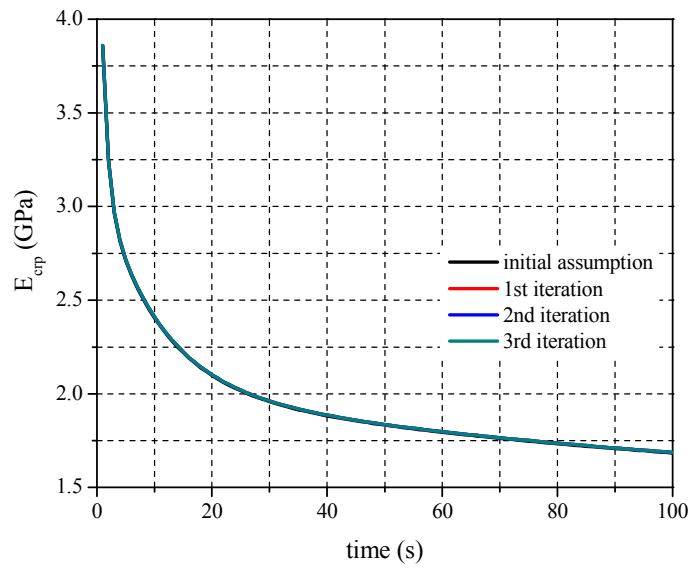


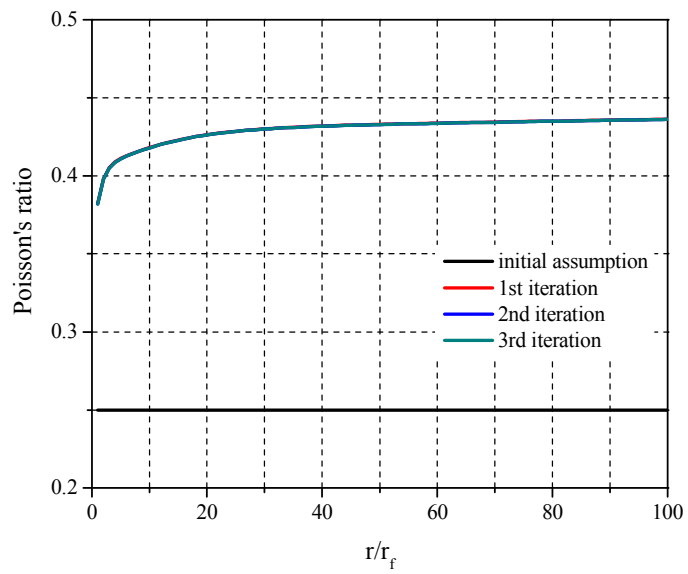
Figure 3.7 Generated BW change

The procedure was implemented, and the results are shown in Figure 3.8. The initially estimated values of E_p by assuming $\nu_p = 0.25$ as well as the values obtained after three iterations are shown in Figure 3.8 (a) and the corresponding values of ν_p are shown in (b).

The percentage errors were calculated by comparing the values obtained from the procedure with the true values, and the results are shown in Figure 3.9. The convergence is extremely fast, and the error becomes negligible even after one iteration, which corroborates the validity of the proposed procedure.



(a)



(b)

Figure 3.8 Obtained (a) Young's modulus and (b) Poisson's ratio by the sequential iterative procedure

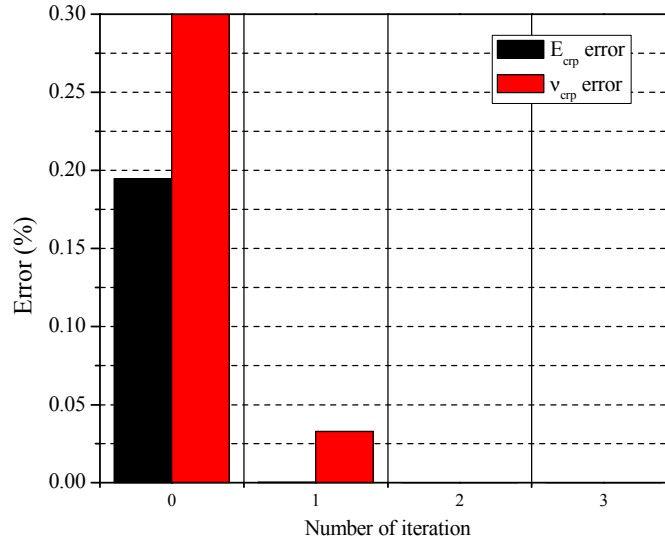


Figure 3.9 Error of the sequential iterative procedure

3.3. Master Curves Under Creep and Stress Relaxation

. From the loading conditions described in the previous section, $E_{crp}(t)$ and $\nu_{crp}(t)$ under creep loading can be obtained at various temperatures, where $E_{crp}(t)$ is a simple reciprocal of the compliance, $J(t)$. Similarly, the creep bulk modulus, $K_{crp}(t)$, which is a simple reciprocal of compressibility or hydrostatic compliance, $J_K(t)$, can be obtained from $E_{crp}(t)$ and $\nu_{crp}(t)$ assuming that the relationship between 4 constants shown in Eqn.(1.1) are valid.

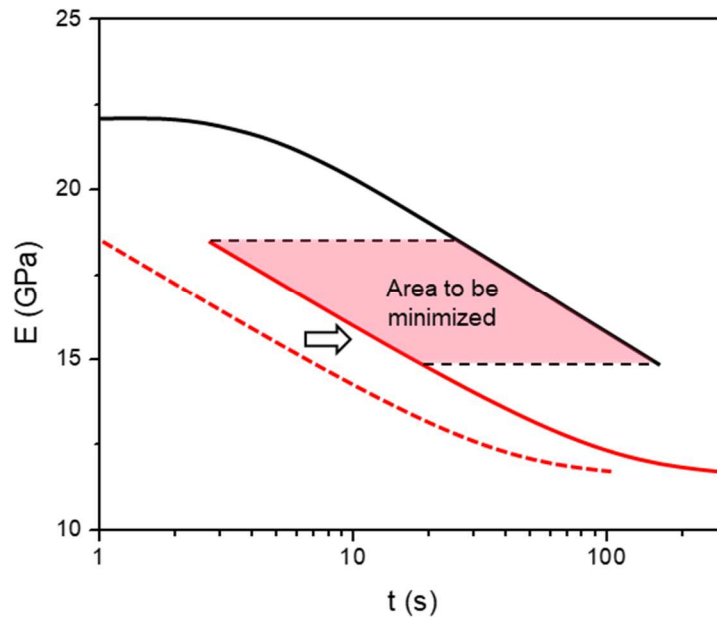


Figure 3.10 Schematic description of shifting algorithm

Adopting the TRS assumption, $E_{crp}(t)$ data can be shifted in the log time scale to construct a master curve of $E_{crp}(t)$ as well as the shift factors, $a(T)$. An automatic shifting routine was developed using the concept illustrated in Figure 3.10. Two sets of $E_{crp}(t)$ obtained at adjacent temperatures are plotted on the log-time scale together. Then, one of the two sets is shifted until the overlapping area is minimized. When this procedure is implemented over the entire temperature range, the master curve for creep compliance and compressibility can be obtained

Once functional forms of $E_{crp}(t)$ and $K_{crp}(t)$ are obtained, the relaxation Young's modulus and bulk modulus, $E(t)$ and $K(t)$, can be obtained using the following convolution relationship.

$$\int_0^t E(t-\tau) \frac{dJ(\tau)}{d\tau} d\tau = 1 \quad (3.6)$$

When the functional form of relaxation modulus is given as a Prony series, each Prony constants can be obtained numerically or analytically [4]. Figure 3.11 shows the results of the convolution using the data shown in Figure 3.6.

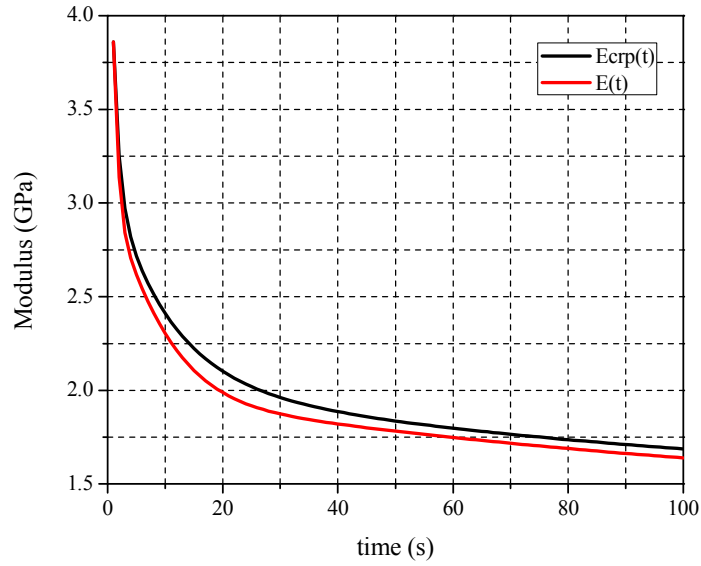


Figure 3.11 $E(t)$ obtained from convolution of $E_{crp}(t)$

Chapter 4 Development of the Testing Setup for the Proposed Method

4.1. Specimen Fabrication

This chapter presents the test setups developed in this study. Three setups are described in detail for (1) specimen fabrication, (2) uniaxial loading, and (3) hydrostatic loading.

4.1. Specimen Fabrication

A stainless-steel mold assembly to cure a cylindrical specimen with embedded FBG is shown schematically in Figure 4.1. The insert shows a plunger that applies the required pressure to the specimen. The optical fiber (diameter of 125 μm) is inserted through a small through-hole drilled in the center of an uncured EMC pellet.

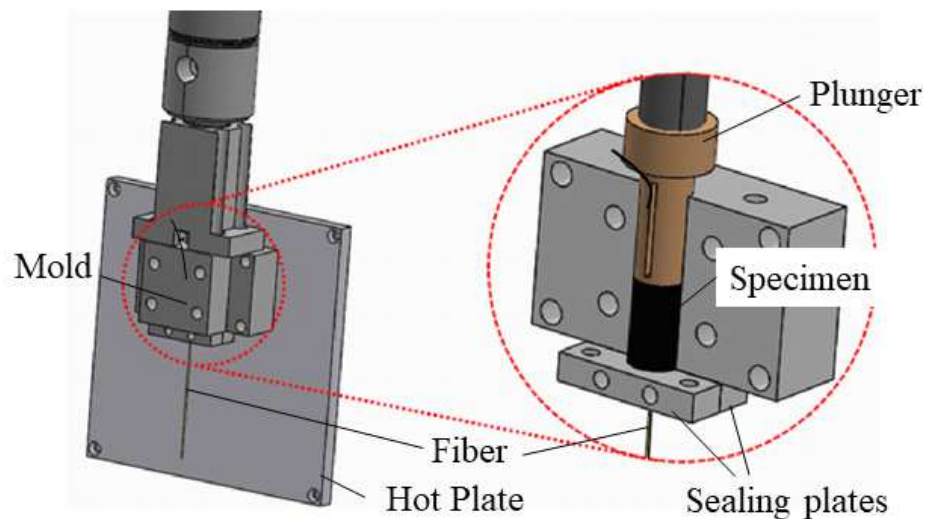


Figure 4.1 Mold assembly to fabricate the EMC specimen

The vertical position of the Bragg grating is adjusted until it is placed in the middle of the pellet. The internal surfaces of the mold are treated with a release agent and thermal grease. The pellet is wrapped with a very thin Teflon tape before the curing process

starts. This pre-processing ensures easy separation after curing as well as no constraint from the mold walls during curing.

A large mechanical pressure has to be applied during curing. The required pressure (7 MPa) is achieved by the mechanical plunger. As illustrated in the insert of Figure 4.1, the plunger is connected to the piston of a pneumatic cylinder. The diameter of the cylinder (31.75 mm) is much larger than the diameter of the plunger (8.9 mm). In this way, the curing pressure is achieved only by an air pressure of 0.54 MPa (78 psi), which is readily available in laboratories.

The complete system is shown in Figure 4.2. The mold (with the pellet) is mounted on a high precision hot/cold plate (HCP304: Instec), which provides temperature control with a resolution of ± 0.05 °C. The compressed air line is connected to the pressure regulator (ER3000: Tescom), which is controlled by a PC to produce a desired air pressure to the air cylinder.

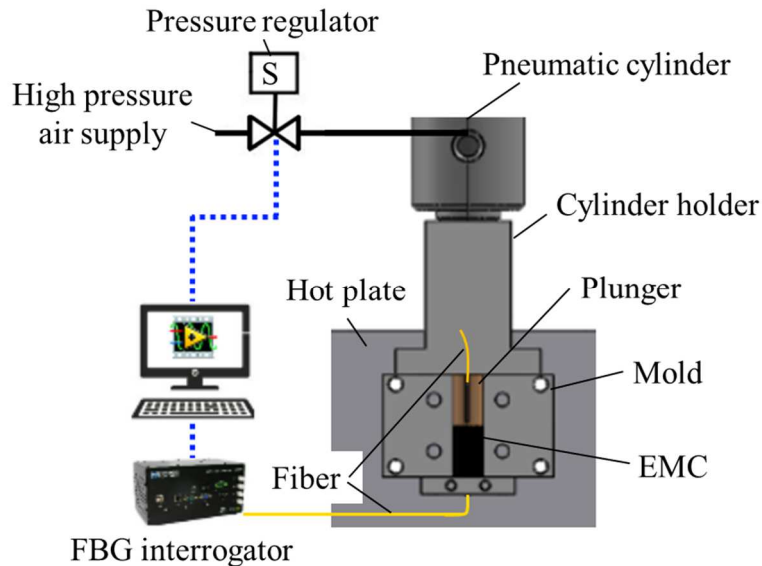


Figure 4.2 Setup for specimen fabrication

After the specimen temperature reaches the curing temperature (175°C), the curing pressure is applied and maintained during curing. The specimen is released from the mold after 5-minute curing time, and it is subsequently subjected to a post mold curing process (for 2 hours at the same temperature without the pressure).

4.2. Uniaxial Test Setup

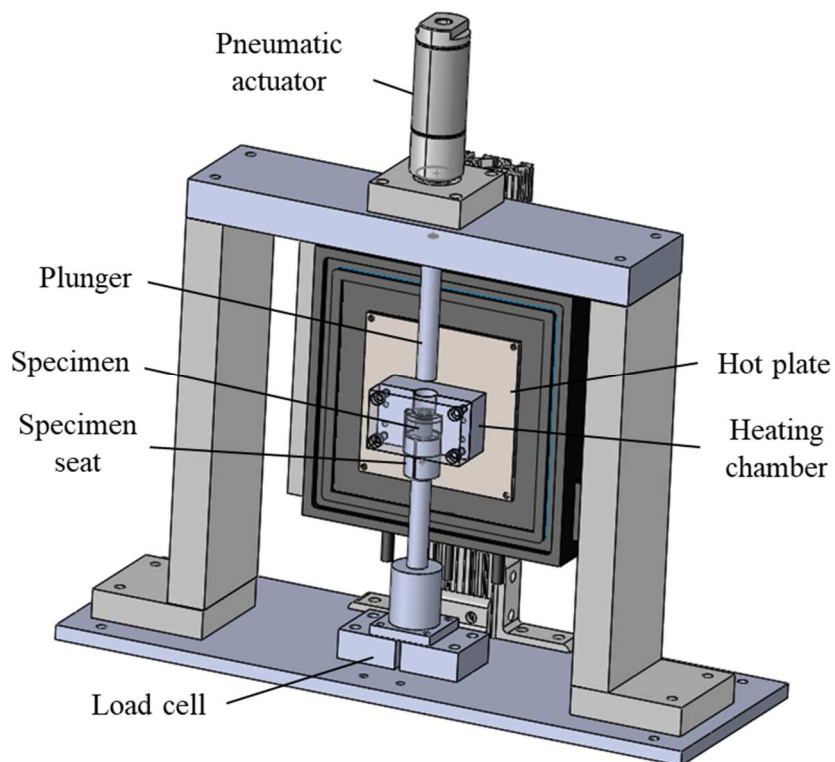
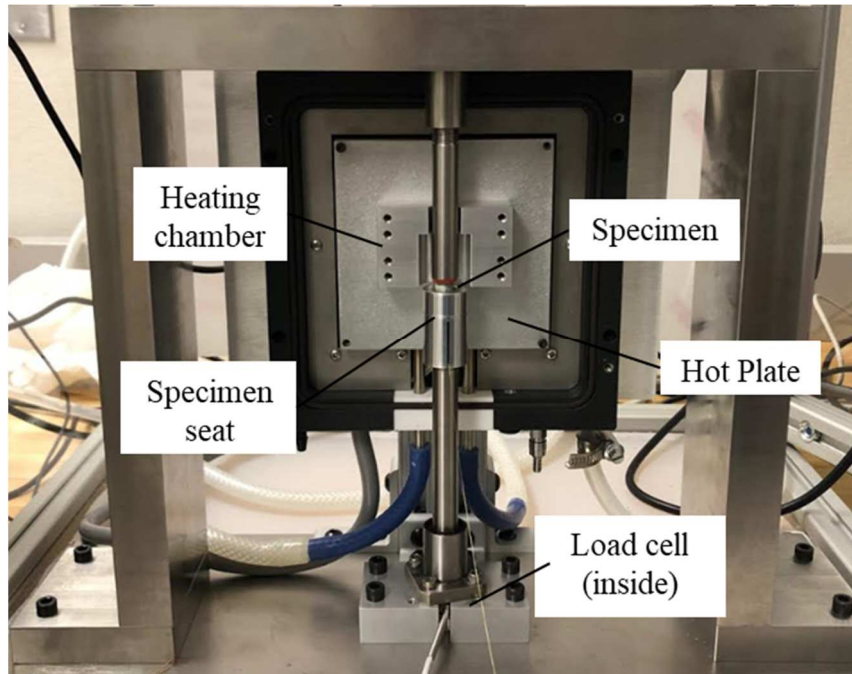
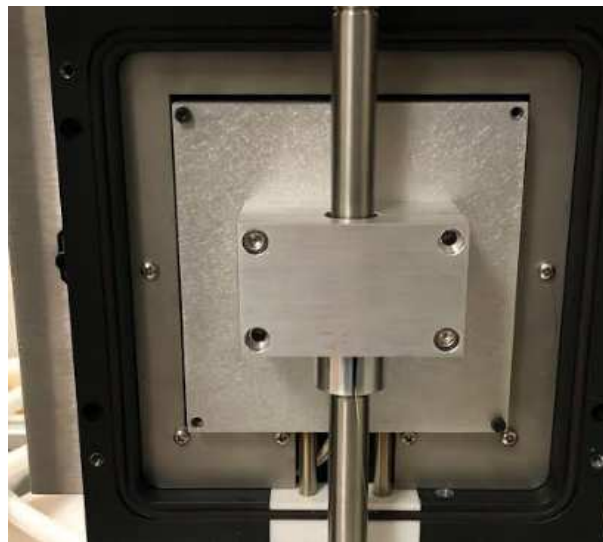


Figure 4.3 Schematic of the uniaxial test setup



(a)



(b)

Figure 4.4 Uniaxial testing setup when (a) heating chamber is open and lifted for setting up and (b) heating chamber is closed and in place for the testing

A schematic diagram of the entire test setup is shown in

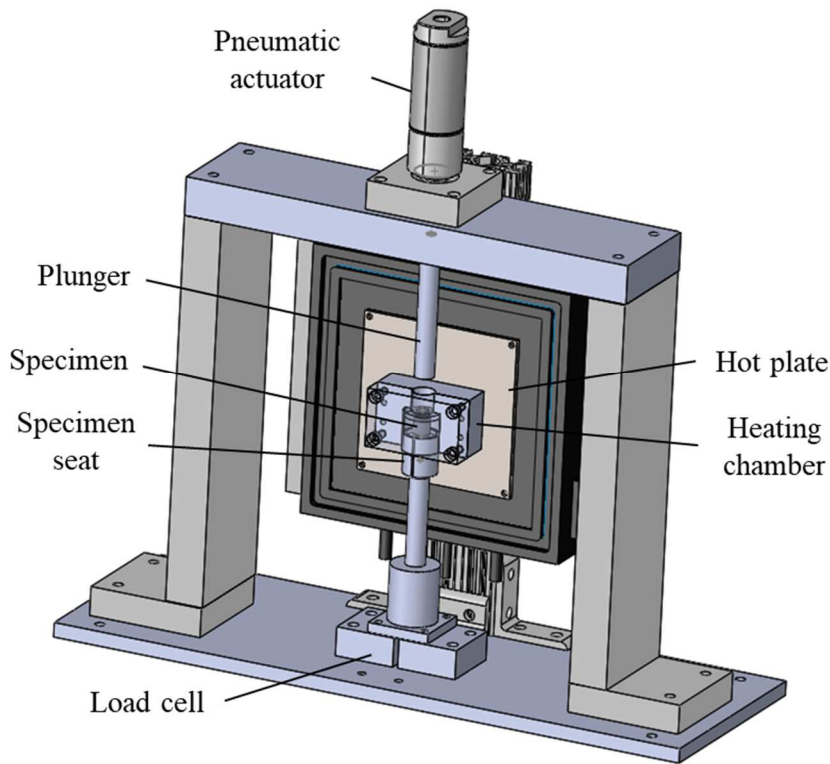


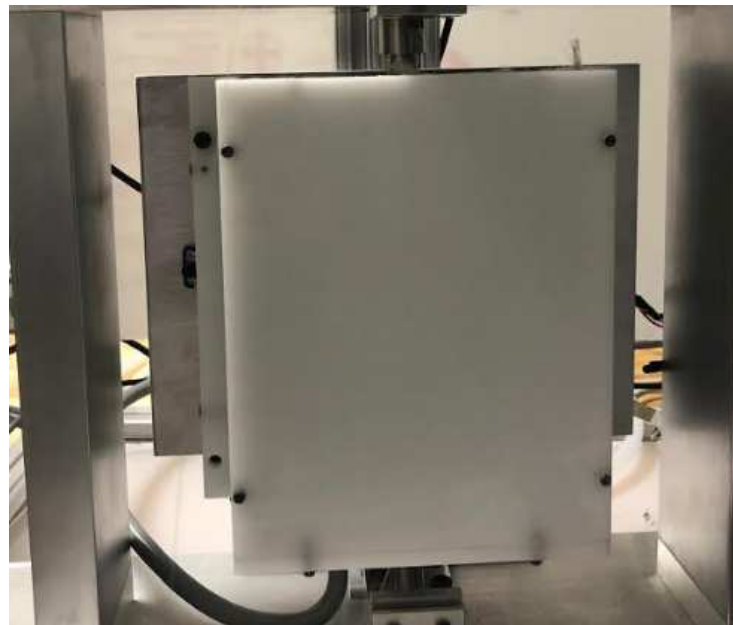
Figure 4.3. The photos of the actual assembly are shown in Figure 4.4. The compressive axial loading is applied by a plunger connected to a pneumatic actuator (CR-141: Bimba), which is actuated by a pressure regulator (ER5000: Tescom). The applied loads are measured by a load cell (Model: Manufacture) placed at the bottom of the setup (Figure 4.4). Pneumatic actuators with various bore diameters can provide a uniaxial loading as large as 6.8 kN.

The temperature control is provided by a precision hot plate (HCP304: Instec). A small chamber which contains the specimen is mounted on the hot plate. After the heating chamber is placed, an insulation box which is a plastic enclosure filled with

layers of high-performance insulation materials covers the entire heating surface to provide faster and uniform heating (Figure 4.5).



(a)



(b)

Figure 4.5 (a) Insulation layers of the insulation cover and (b) insulation cover covering entire heated parts of the testing setup

An EMC specimen with an embedded thermocouple was fabricated and used to check the performance of the temperature control unit. An additional thermocouple was attached to the top and the bottom surface of the specimen during the test. The results are shown in Figure 4.6. The center of the specimen showed the highest temperature and the temperature difference between the top and the center of the specimen was only 0.7 °C and the difference between the bottom and the center of the specimen was only 0.5 °C

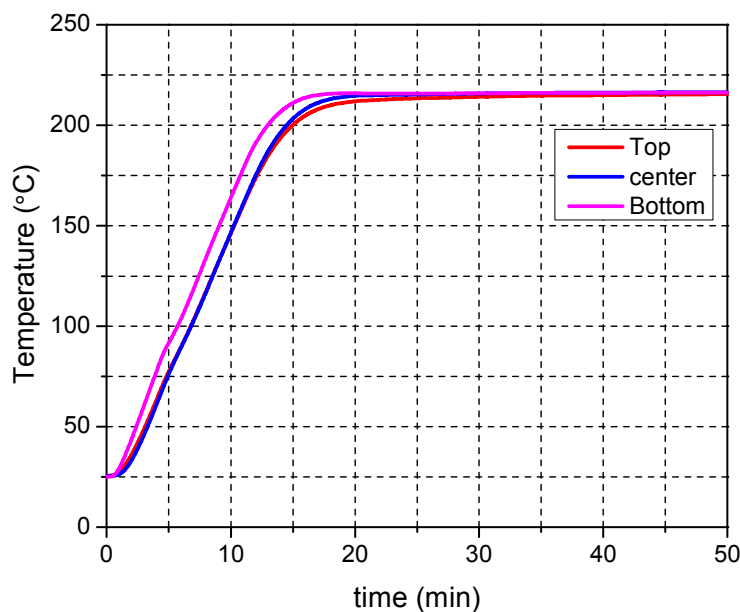


Figure 4.6 Testing heating capability to confirm the temperature uniformity within the specimen

The most important advantage of the load train is a fast rate of loading provided by the gas system, which is critical to creep testing. Figure 4.7 shows a data obtained by the fastest loading rate achieved by the system. It was obtained by suddenly opening

the inlet solenoid valve of the regulator that is connected to an air supply (110 psi). It took about 60 ms to reach a target load of 180 N which corresponds to the highest required loading level for the test.

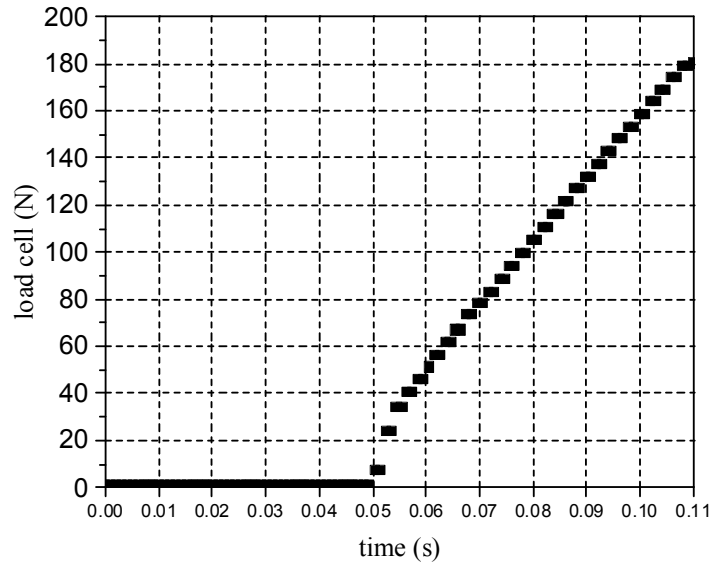


Figure 4.7 Fastest loading from the setup

The current setup provides a loading rate as large as approximately 3,000 N/s. A long-term stability of loading was also tested. Three load levels were tested, and the results are shown in Figure 4.8

The representative uniaxial creep data obtained at 25°C, 125°C and 175°C are shown in Figure 4.9, where the BW change (ΔBW) is normalized by the applied stress. The constant BW before loading confirms the temperature stability of the specimen achieved during testing.

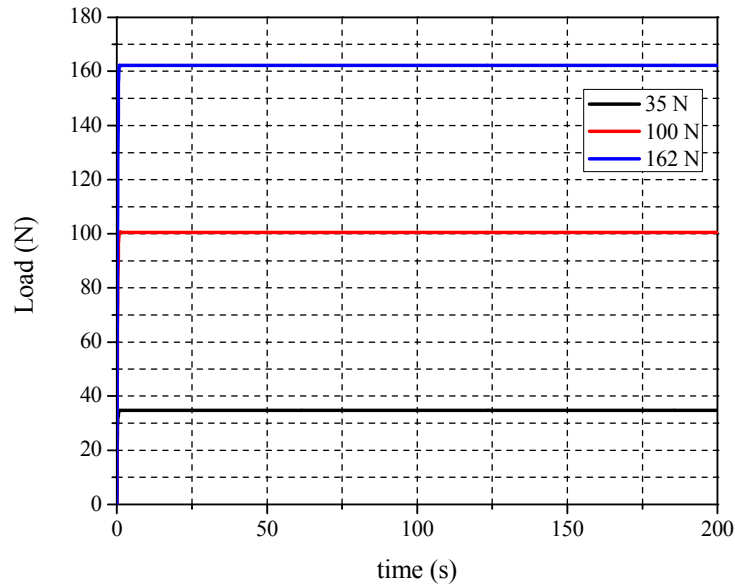
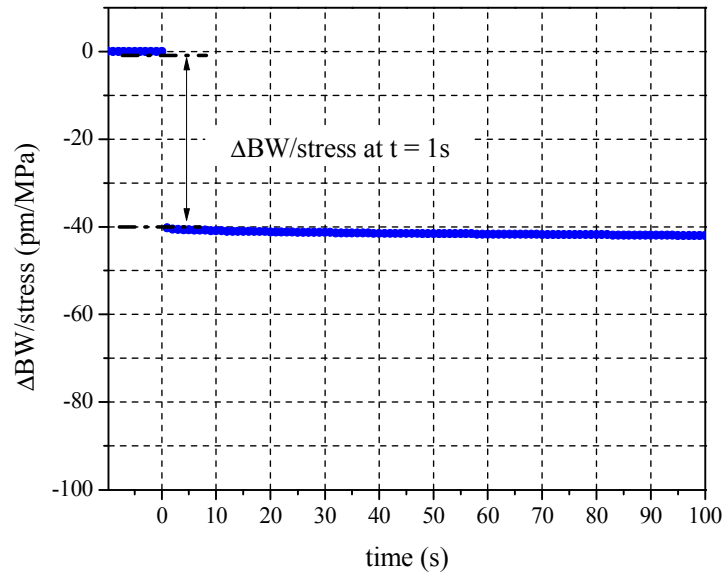
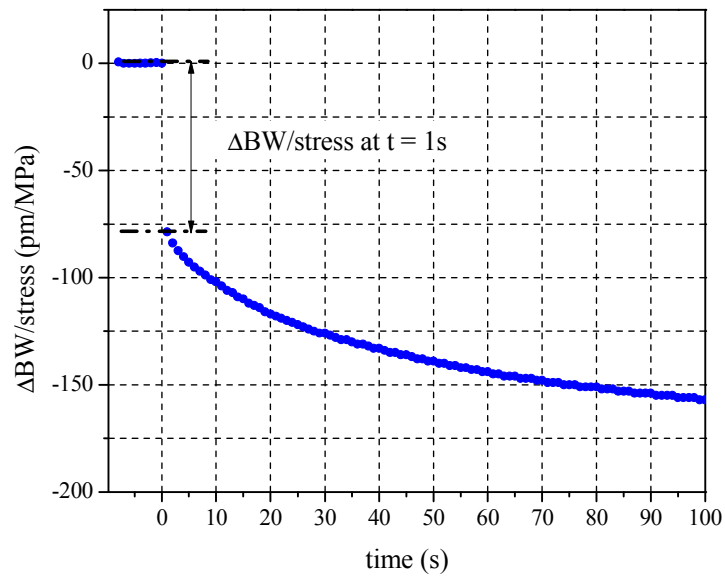


Figure 4.8 Long term loading stability test

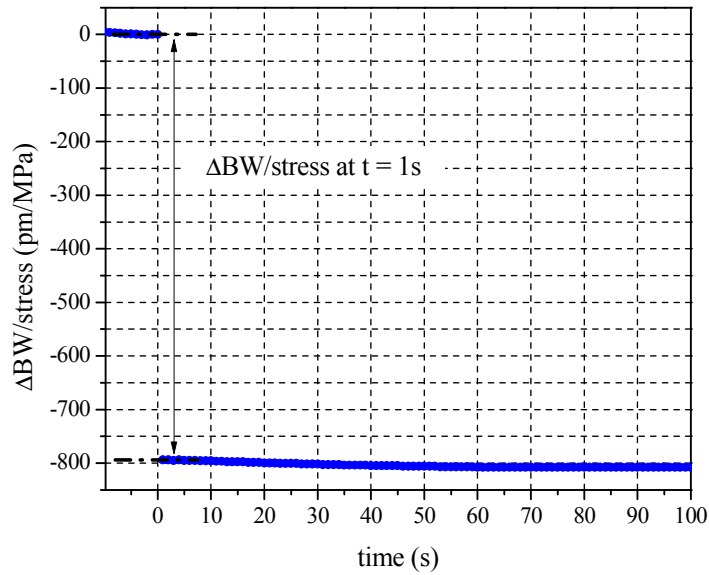
The spectral response of the FBG was also recorded and examined to ensure no spectral distortion during the loading, which would be an indication of non-uniform loading. There was no spectral distortion observed before and after the test as shown in Figure 4.10. It should be noted that, at temperatures 25°C and 175°C, which were below and above glass transition temperature, respectively, the BW remained constant after the load was applied, which indicated that the modulus was virtually time independent. At 125°C, which lay within the glass transition range, however, the BW continued to decrease after the load was applied due to the significant time-dependent behavior of the EMC.



(a)



(b)



(c)

Figure 4.9 BW changes normalized by the applied uniaxial compressive stress at (a) 25 °C, (b) 125 °C and (c) 175 °C

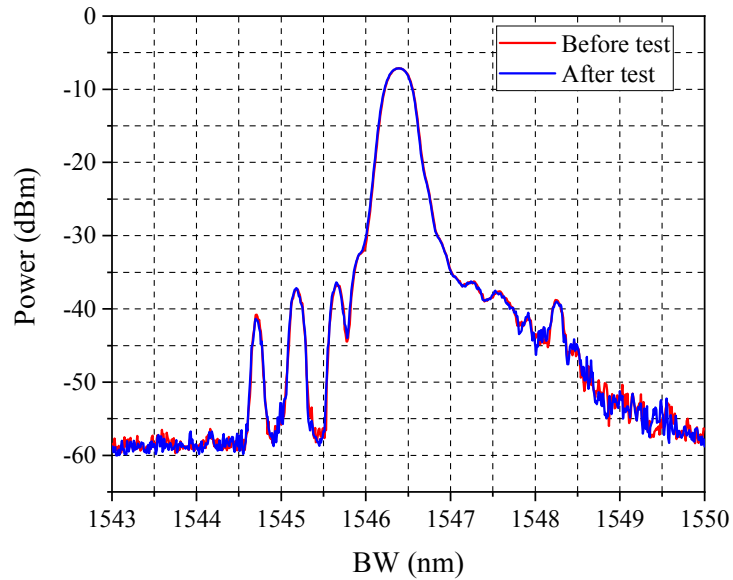


Figure 4.10 Reflected signal spectrum before and after the test

4.3. Hydrostatic Test Setup

A higher gas pressure is required for hydrostatic pressure testing simply because it is more difficult to deform the specimen under hydrostatic pressure. A small test chamber is designed to accommodate the required high gas pressure. As shown in Figure 4.11, the specimen is placed inside the chamber, which has a slightly larger internal area than the specimen does.

The chamber has to be sealed completely while allowing the fiber to be connected to the interrogator. A special sealing system is used to achieve the requirements. The compressive sealing subassembly is shown schematically in Figure 4.12.

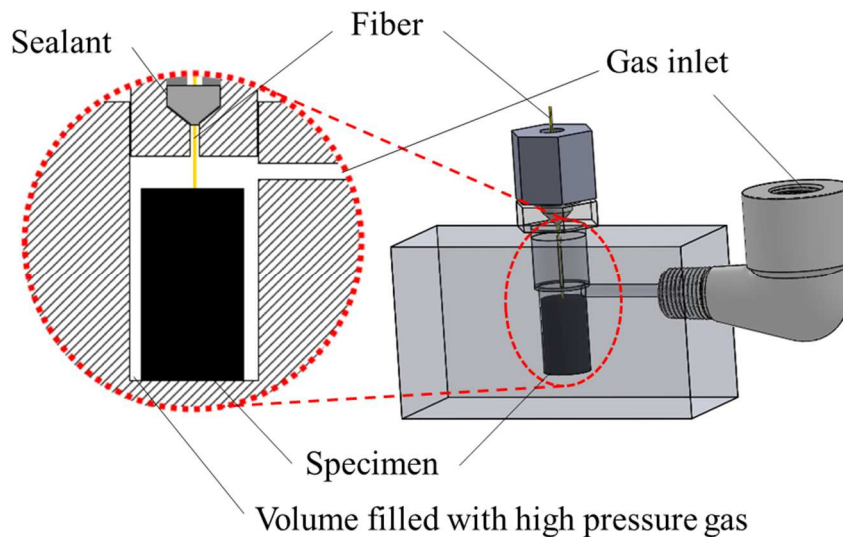


Figure 4.11 Hydrostatic Test Setup

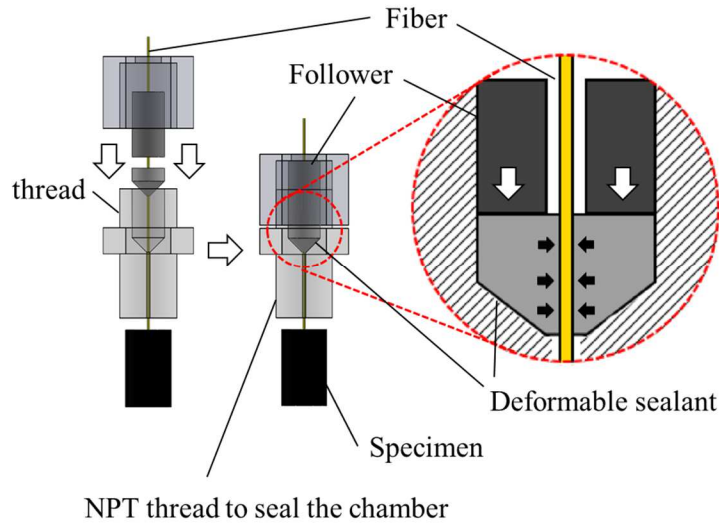
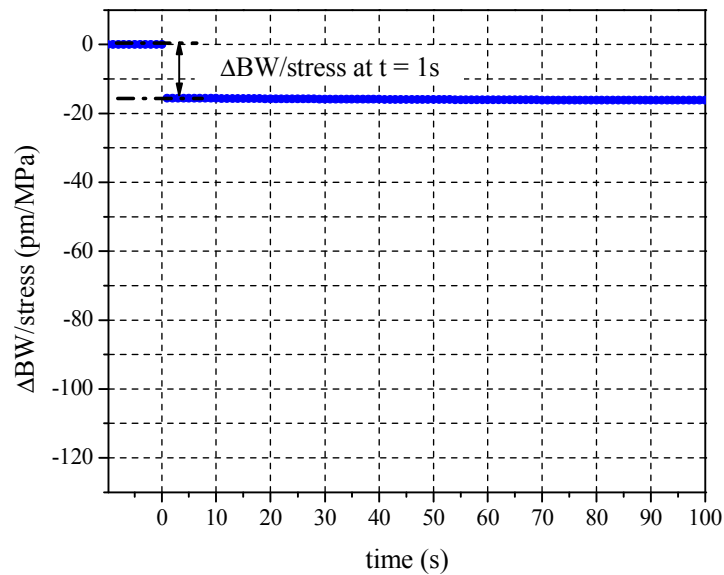


Figure 4.12 Compression sealing for the optical fiber

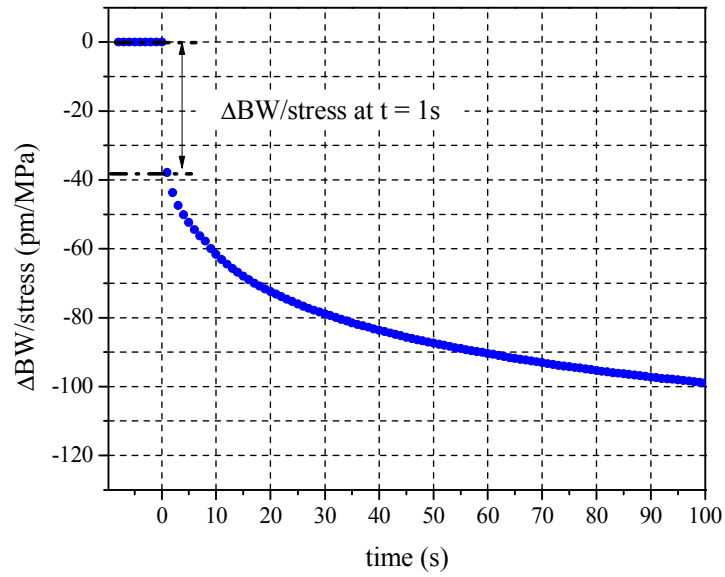
The fiber passes through the system, which utilizes a deformable (Teflon) sealant to seal the fiber (see the insert). The chamber is mounted on the same heating stage used for the uniaxial test shown in Figure 4.4. The gas inlet of the chamber is connected to a regulator of a Argon tank. The Argon tank provides a gas pressure of approximately 15.2 MPa. The output gas from the tank passes through a main regulator (26-2015: Tescom). The main regulator is controlled by a pilot controller (ER5000: Tescom) with a transducer (100-1500: Tescom) that provides a pressure feedback to the computer. The output pressure to the test chamber can be controlled with an accuracy of ≈ 6.9 KPa, and the target pressure is reached within 1s. The maximum pressure output to the test chamber is 6.9 MPa. It should be noted that heat is generated immediately after the target pressure is applied to the test chamber since the gas present (i.e., air) in the chamber is suddenly compressed. This undesired heat causes thermal expansion of the specimen, which offsets the hydrostatic strain of the specimen. The

effect of the heat generation is virtually negated by making the net volume of the compressed gas smaller than 900 mm³.

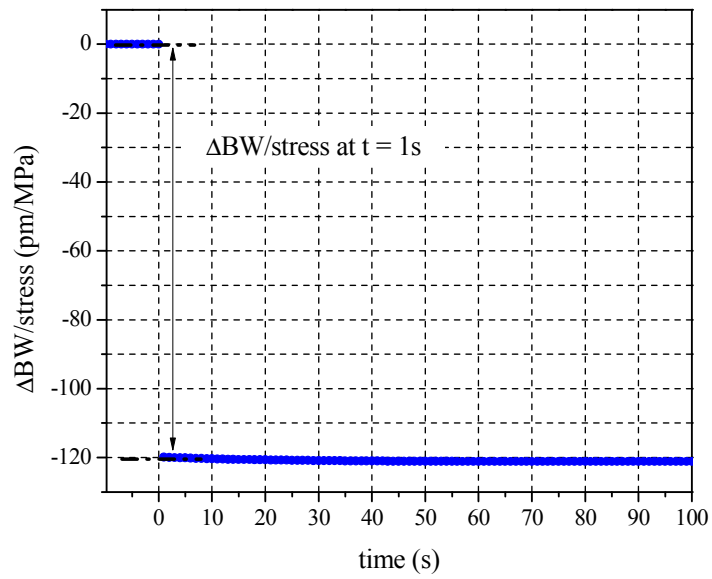
The representative hydrostatic creep data obtained at 25°C, 125°C and 175°C are shown in Figure 4.13, where the BW change (ΔBW) is normalized by the applied stress. Again the constant BW before loading confirms the temperature stability of the specimen achieved during testing.



(a)



(b)



(c)

Figure 4.13 BW changes normalized by the applied hydrostatic stress at (a) 25 °C, (b) 125 °C and (c) 175 °C

Chapter 5 Measurement Result of Two Time Dependent Elastic Moduli

An EMC specimen was tested from 25 °C to 235 °C. The temperature interval between measurements was 20 °C below and above the glass transition temperature, and 5 °C over the glass transition range. Temperature interval is chosen to ensure the enough measuring point for the shift factor to be fitted into a functional.

In the uniaxial compression test, three different stresses of 4.98 MPa, 1.8 MPa and 0.18 MPa were used for the temperatures below, near and above the glass transition temperature, respectively in order to incorporate the strong temperature-dependent behavior; the corresponding air cylinder pressures were 344.7 KPa, 137.9 KPa, 13.8 KPa, respectively. Hydrostatic creep testing was conducted at the same temperatures. Two different pressures of 6.9 MPa and 1.4 MPa were applied for the temperatures below and above the glass transition temperature, respectively. The rule to determine the applied pressure is that initial BW change should be at least 100 pm considering the accuracy (1pm) of the FBG interrogator. Raw data from uniaxial and hydrostatic creep tests are shown in Figure 5.1 and Figure 5.2, respectively. Largest BW change is around 300 pm at which the expected strain of the specimen is less than 0.03%. Therefore, it is safe to assume that the specimen is in linear viscoelastic region. Data is saved with 1 Hz frequency and number of data point on figures is reduced for visualization purpose.

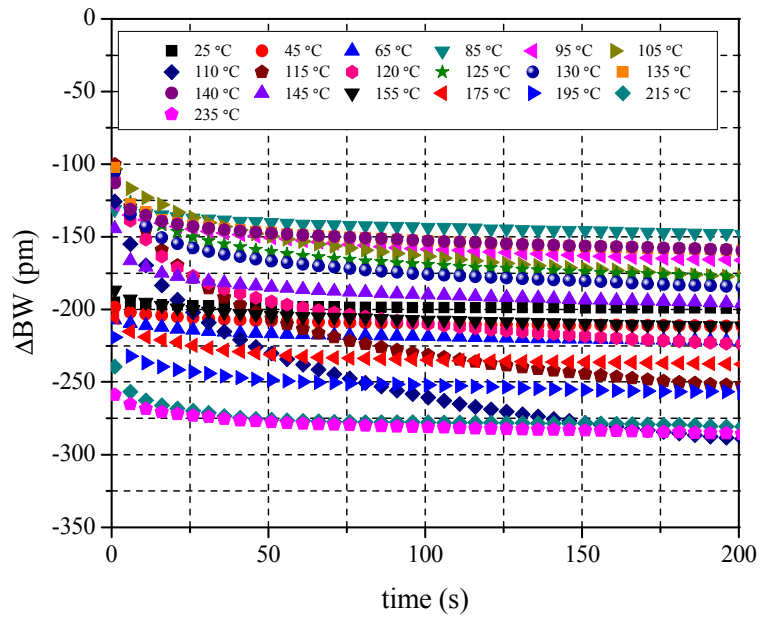


Figure 5.1 Raw Bragg wavelength change from uniaxial creep test

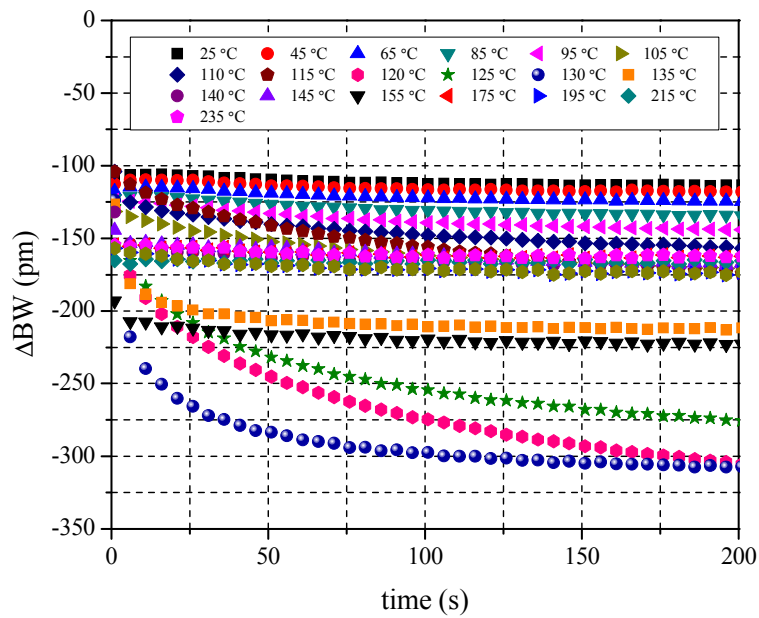


Figure 5.2 Raw Bragg wavelength change from hydrostatic creep test

The data from uniaxial and hydrostatic creep tests from each temperature were used to obtain time dependent creep compliance $J(t)$ and creep Poisson's ratio $\nu_{crp}(t)$ at each temperature using the sequential iterative procedure presented in the previous chapter. Figure 5.3 shows the compliance calculated as a function of time at each temperature and shifted to form a master curve using the procedure presented in chapter 3. Figure 5.4 shows the shift factor obtained from the compliance. The same shift factors were used to produce the master curve of the compressibility as shown in Figure 5.5

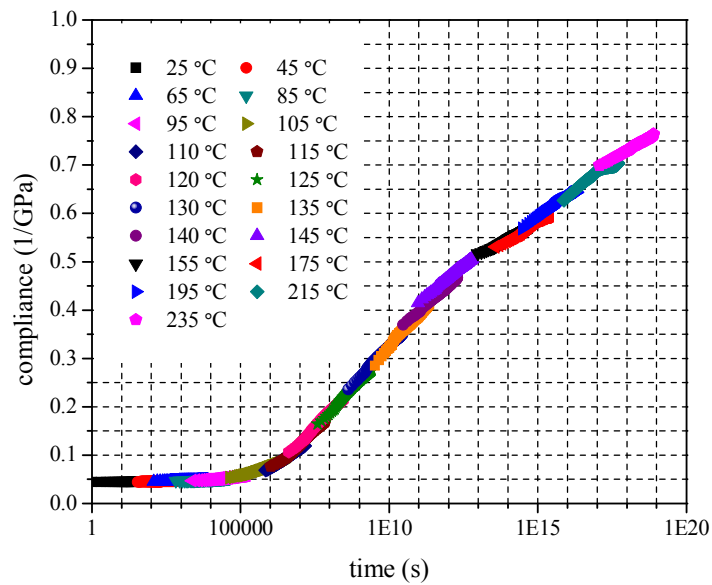


Figure 5.3 Compliance at various temperatures and shifted to obtain shift factors

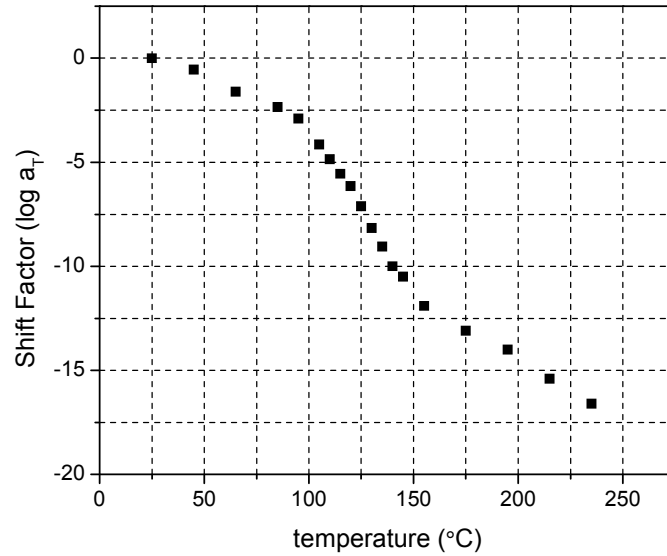


Figure 5.4 Shift factors obtained from shifting compliance

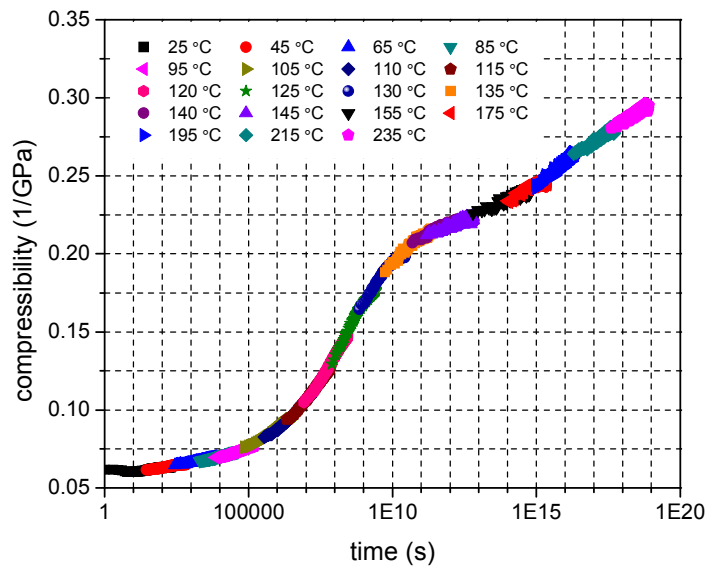


Figure 5.5 Compressibility at each temperature shifted using shift factors obtained from compliance result

The compliance and compressibility can be fitted into the following functional forms.

$$J(t) = J_0 + \sum_{i=1}^n J_i \left(1 - \exp\left(-\frac{t}{\tau_i}\right) \right) \quad (5.1)$$

$$J_K(t) = J_{K,0} + \sum_{i=1}^n J_{K,i} \left(1 - \exp\left(-\frac{t}{\tau_i}\right) \right)$$

Figure 5.6 and Figure 5.7 show the compliance and compressibility fitted into the functional form.

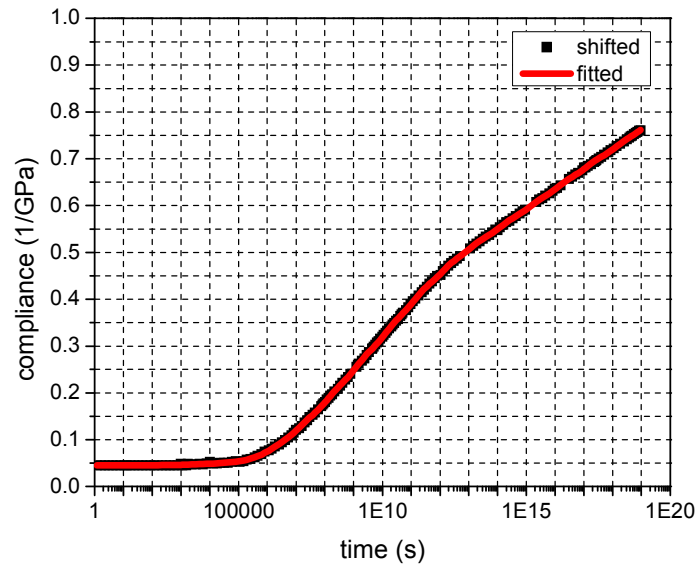


Figure 5.6 Creep compliance fitted into a functional form

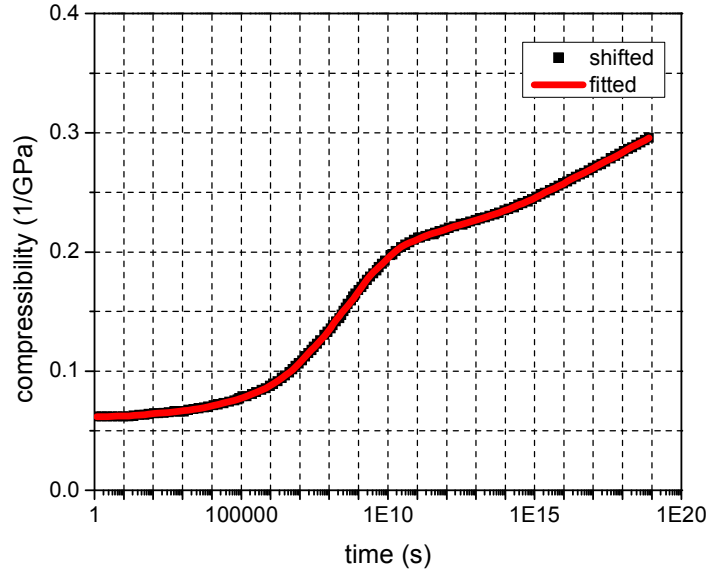


Figure 5.7 Creep compressibility fitted into a functional form

The relaxation Young's modulus and bulk modulus can be obtained from them using the convolution equations, repeated here.

$$\begin{aligned}
 t &= \int_0^t E(t-\tau)J(\tau)d\tau \\
 t &= \int_0^t K(t-\tau)J_K(\tau)d\tau
 \end{aligned}
 \tag{5.2}$$

It can be done numerically or analytically when both compliance and relaxation moduli are expressed as Prony series as:

$$\begin{aligned}
 E(t) &= E_\infty + \sum_{i=1}^{20} E_i \exp\left(-\frac{t}{\tau_i}\right) \\
 K(t) &= K_\infty + \sum_{i=1}^{20} K_i \exp\left(-\frac{t}{\tau_i}\right)
 \end{aligned}
 \tag{5.3}$$

For numerical analyses using commercial packages, the relaxation shear modulus and bulk modulus are required as an input data. The shear modulus can be calculated from the Young's modulus and bulk modulus and can be fitted into the following Prony series.

$$G(t) = G_{\infty} + \sum_{i=1}^{20} G_i \exp\left(-\frac{t}{\tau_i}\right) \quad (5.4)$$

A single shift function to fit the whole set of shift factors is difficult, especially when a very large temperature range is to be considered. The small discrepancy between the experimentally obtained shift factors and the fitted value can cause a large error in the implementation since the time axis of the master curve is in the log scale.

The Williams–Landel–Ferry (WLF) model is the most widely used function for the shift factors [30]. It is based on the free volume theory; it has been known that the WLF function is more effective for the temperature around T_g [31-33]. The Arrhenius equation can be used for the shift factors. It is an empirical equation; it has been known that the Arrhenius shift function is valid only for $T < T_g$. [5, 10, 32].

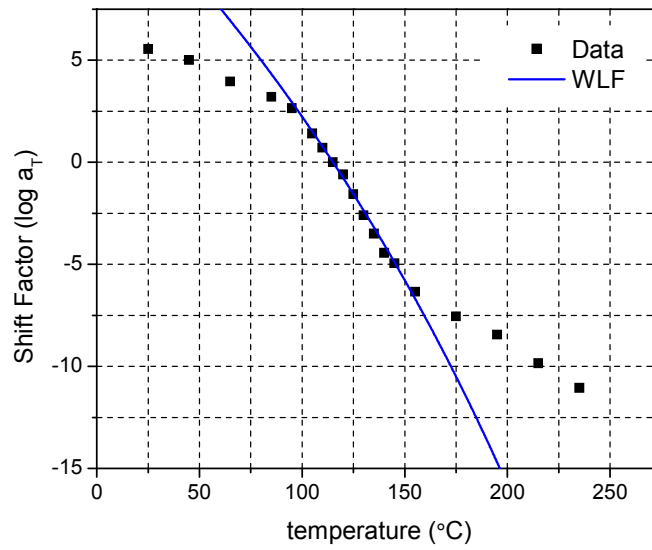
In this study, a piecewise shift function is proposed to fit the shift factors. The WLF function is used for the temperatures in the glass transition range. Two polynomial functions are used to accommodate the temperatures below and above glass transition temperature. The piecewise shift function can be expressed as:

$$\begin{aligned} \log a_T^{p1}(T) &= a_0 + a_1(T-115) + a_2(T-115)^2 + a_3(T-115)^3 \quad \text{for } T \leq 115^\circ C \\ \log a_T^{WLF}(T) &= -\frac{C_1(T-130)}{C_2 + (T-130)} \quad \text{for } 115^\circ C \leq T \leq 145^\circ C \\ \log a_T^{p2}(T) &= b_0 + b_1(T-145) + b_2(T-145)^2 + b_3(T-145)^3 \quad \text{for } T \geq 145^\circ C \end{aligned} \quad (5.5)$$

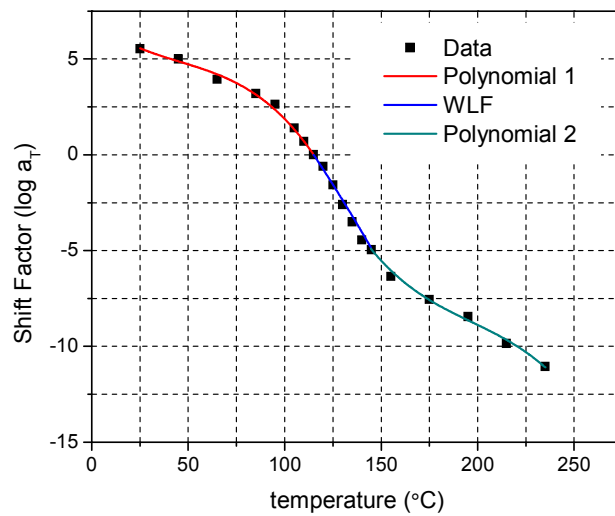
where $\log a_T^{p1}$ and $\log a_T^{p2}$ are the polynomial shift functions for the temperatures below and above the glass transition range; and a_T^{WLF} is the WLF function for the temperatures of the glass transition range. It is to be noted that $a_0 = \log a_T^{WLF}(115)$ and $b_0 = \log a_T^{WLF}(145)$, which makes the piecewise shift function continuous. The function is empirical but can accommodate more than one temperature range. The constants of Eq. (5.5) are:

$$\begin{aligned} a_1 &= -0.148; a_2 = -1.72 \cdot 10^{-3}; a_3 = -8.09 \cdot 10^{-6}; \\ C_1 &= -73.36; C_2 = -479.0; \\ b_0 &= -4.95; b_1 = -0.122; b_2 = 1.44 \cdot 10^{-3}; b_3 = -9.22 \cdot 10^{-6} \end{aligned}$$

The results of the piecewise shift function are shown in Figure 5.8. The shift factors over the entire temperature range are represented accurately by the piecewise shift function. A single WLF function that represents the entire shift factors is also shown in Figure 5.8. It is evident that a single WLF function should not be used for the entire temperature range. Otherwise, it would be prone to large errors in shift factor calculations.



(a)



(b)

Figure 5.8 Shift factors fitted into (a) single WLF function and (b) piece-wise Shift functions

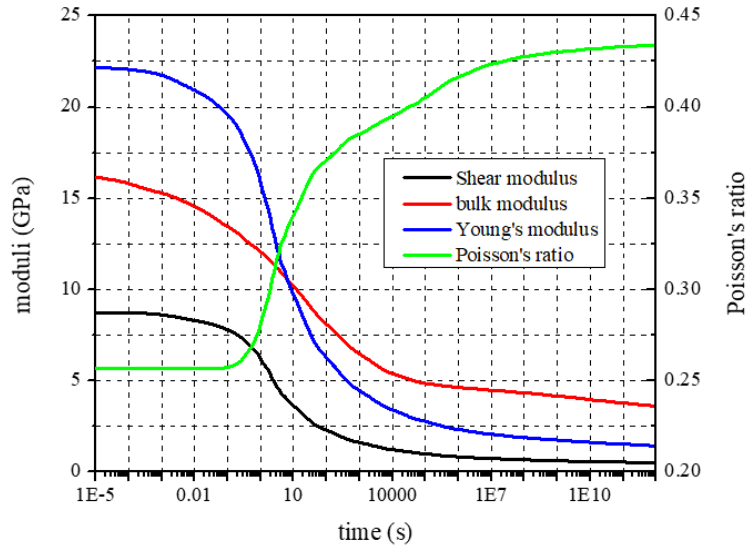


Figure 5.9 Master curve of four time-dependent constants (reference temperature: 115 °C)

Figure 5.9 shows the master curves of relaxation shear, bulk, and Young's modulus as well as the Poisson's ratio, where the reference temperature is 115 °C. The corresponding Prony series coefficients of shear and bulk modulus are shown in Table

1

Table 1 Prony coefficients for shear and bulk moduli master curves

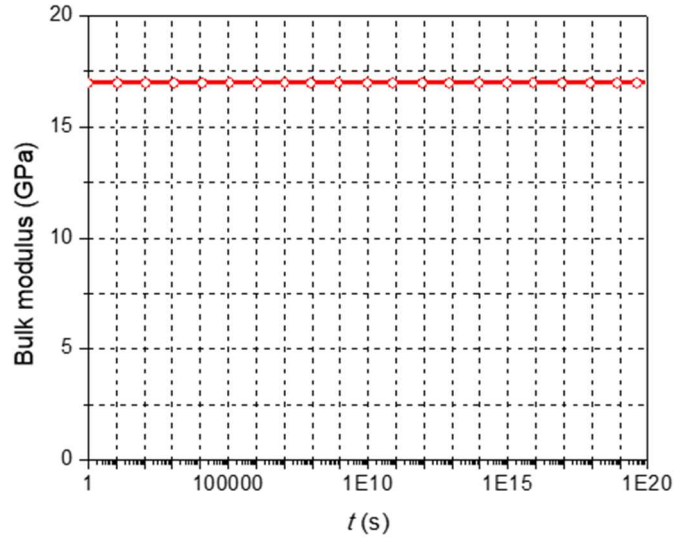
| i | K_i | G_i | τ_i |
|----------|----------|----------|----------|
| ∞ | 3.010215 | 0.645561 | - |
| 1 | 0.236133 | 0.143006 | 2.82E-06 |
| 2 | 0.183344 | 0.286667 | 1.41E-05 |
| 3 | 0.349821 | 0.070826 | 2.82E-05 |
| 4 | 0.127797 | 0.238421 | 0.000282 |
| 5 | 0.275802 | 0.512541 | 0.002818 |
| 6 | 0.100651 | 0.769152 | 0.028184 |
| 7 | 0.067098 | 0.701428 | 0.281838 |
| 8 | 0.310034 | 0.368043 | 2.818383 |
| 9 | 0.429831 | 0.368581 | 28.18383 |
| 10 | 0.281981 | 3.336293 | 281.8383 |
| 11 | 0.847911 | 3.147961 | 2818.383 |
| 12 | 1.113954 | 4.76305 | 28183.83 |
| 13 | 1.979667 | 4.758096 | 281838.3 |
| 14 | 3.584168 | 3.135874 | 2818383 |
| 15 | 2.516805 | 1.680549 | 28183829 |
| 16 | 0.727437 | 0.62975 | 2.82E+08 |
| 17 | 0.165545 | 0.448752 | 2.82E+09 |
| 18 | 0.075488 | 0.185135 | 2.82E+10 |
| 19 | 0.061471 | 0.280286 | 2.82E+11 |
| 20 | 0.053267 | 0.258061 | 2.82E+12 |
| 21 | 0.071814 | 0.132094 | 2.82E+13 |
| 22 | 0.079516 | 0.387392 | 2.82E+14 |

Chapter 6 Effect of Constant Bulk Modulus and Poisson's ratio on Thermal Stress Analysis

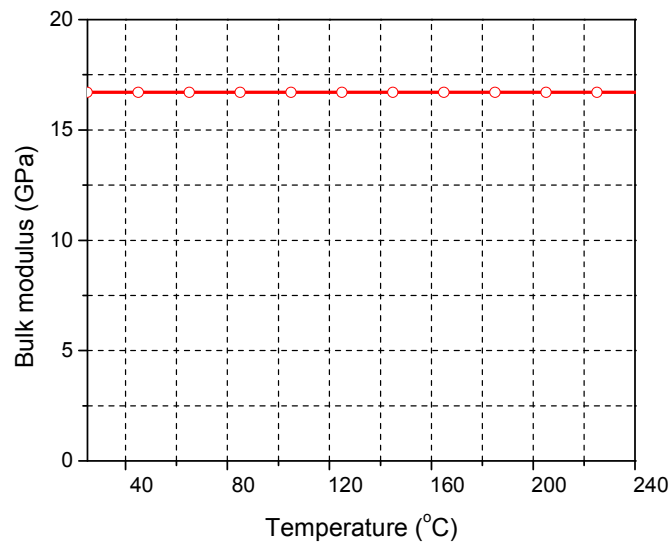
Time-independent Bulk modulus and constant Poisson's ratio are commonly used assumption for thermal stress analysis of packages to reduce development cost. Their effect on stress analysis is discussed with examples.

6.1. Effect of Time-dependent Bulk Modulus on Reliability Assessment of Automotive Electronic Control Unit

One of the advanced electronics that have been adopted in automotive technologies to enhance user interfaces is an automotive electronic control unit (ECU), which is an embedded system that controls an electrical system or subsystems in a transport vehicle. In a conventional ECU, a protective metal case has been used to ensure reliability under harsh environmental conditions. Recently, the EMC has been adopted to replace the metal case. The EMC technology reduced a manufacturing cost significantly, yet the presence of a large amount of outer EMC can increase the stresses of ECUs during the transfer molding process and operations. The temperatures of the manufacturing process and the operating conditions of ECUs are higher than the glass transition temperature of the EMC, and thus, the time-dependent bulk modulus should be considered in stress prediction unless its effect is negligible.



(a)



(b)

Figure 6.1 Implication of the assumption of bulk modulus behavior: (a) temperature-independent; and (b) time-independent

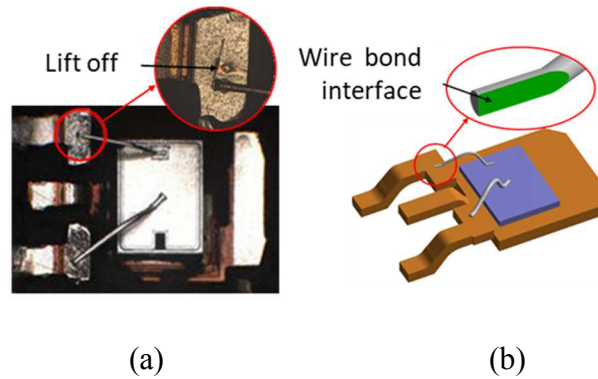


Figure 6.2 (a) Wirebond “lift-off” failure in a DPAK, and (b) Al wire bond interface of interest [9]

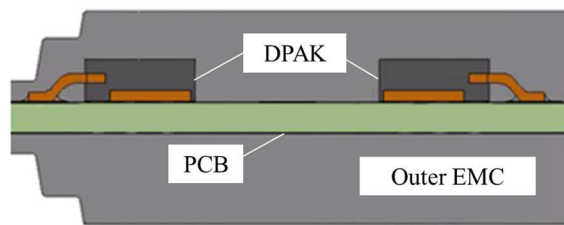


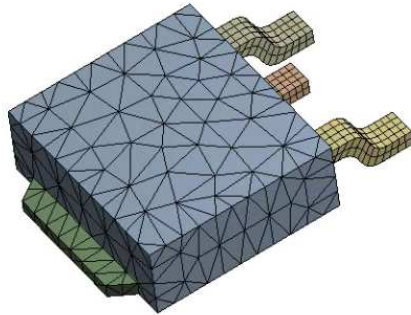
Figure 6.3 Schematic cross-sectional view of the FEA model to simulate the presence of the outer mold [9]

It is important to recall that the assumption of “time-independent” bulk modulus implies that the bulk modulus becomes “temperature-independent” if EMC behavior follows the TRS assumption. These implications are illustrated in Figure 6.1.

An over molded ECU package is used to investigate the effect of the time dependent bulk modulus. The stress model for the outer mold and also DPAK package inside the ECU is investigated. Several failure modes are known in the DPAK molded inside an ECU. They include delamination between molding compound and copper lead frame, wire bond failure, and solder joint failure [5]. One of the most common failure modes is wire lift-off in power electronic devices [6-8]. Figure 6.2(a) illustrates

the interfacial delamination between the gate Al wire and Cu lead inside a molded ECU after a series of thermal cycling tests. The interface between an aluminum wire bond and metal pad shown in Figure 6.2 (b) is selected to investigate the effect of the bulk modulus.

The schematic of the cross-section of the molded ECU package used in the analysis is shown in Figure 6.3. The validity of the model was verified by Moiré interferometry in Ref. [9].



(a)



(b)

Figure 6.4 FEA models of DPAK in ECU unit shown (a) with EMC (b) without EMC

A DPAK package overmolded by outer mold has been investigated using time-dependent and independent bulk modulus [10]. The DPAK package model shown in

Figure 6.4 was subjected to a thermal loading (heating from 25 to 240 °C) with two different bulk moduli: (1) temperature-dependent bulk modulus and (2) constant bulk modulus.

Normal stresses at the wire bond interface were analyzed to investigate the effect of the lift-off failure. The maximum normal stress was determined first with the temperature-dependent bulk modulus, and then it was compared with the case of the constant bulk modulus. When the constant K was used, the maximum normal stress at the interface increased by 9.2 %.

The same thermal loading condition was applied to the DPAK molded by an outer EMC for the comparison purpose, different properties with and without the constant bulk modulus assumption was applied to the molding compound of DPAK.

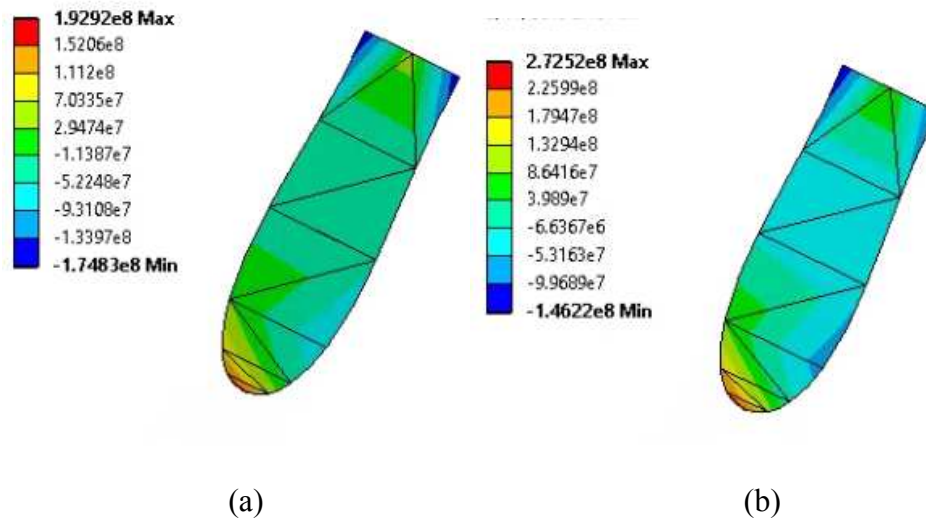


Figure 6.5 Comparison of wire bond interface stresses (a) without the constant bulk modulus assumption and (b) with the assumption

The stresses of the bonding wire for two cases are shown in Figure 6.5. The maximum normal stress at the wire bond interface increased by 41.2% when the constant bulk modulus was used. It is attributed to the fact that DPAK EMC was

constrained excessively with the outer mold. The result clearly shows that the DPAK EMC with a constant bulk modulus can constrain the package excessively, which results in significantly overestimated stresses in the package. This result clearly shows that the constant bulk modulus assumption may affect the reliability of a package significantly depending on the application.

6.2. Effect of Constant Poisson's ratio on Warpage Analysis

To accommodate demands for reducing development cycle, temperature-dependent linear elastic stress analysis is often used to predict the package behavior approximately. An elastic stress analysis of semiconductor packages requires temperature-dependent Young's modulus and Poisson's ratio. It is relatively easy to measure Young's modulus; the temperature-dependent Young's moduli are measured routinely by commercial instruments, e.g., dynamic mechanical analyzer (DMA), universal tensile testing machine (UTTM), etc. The Poisson's ratio is, however, more difficult to measure because the measurement requires two strains - axial strain and transverse strain. Obtaining the two strains accurately as a function of temperature is not a trivial task.

The effect of Poisson's ratio can be large when thermosetting polymers in packages are subjected to multiaxial constraints. Even when the critical deformations such as the maximum stresses, the maximum warpage, etc., are sensitive to Poisson's ratio, a parametric study can still be performed without losing generality as long as relative evaluations among various designs or loading conditions are sought. For this

very reason, a constant Poisson's ratio estimated at room temperature is typically used for the elastic stress analysis.

If an absolute stress or warpage is to be predicted, however, it is inevitable to use temperature-dependent Poisson's ratio. This becomes more critical if the maximum temperature of thermal loading exceeds the glass transition temperature of polymers.

In this section, the effect of Poisson's ratio on the elastic stress analysis of packages containing thermosetting polymers is investigated by two case studies, where the polymers are subjected to multiaxial constraints.

A semiconductor package is a composite structure with various materials bonded together. The stresses within the package are caused by the coefficient of thermal expansion (CTE) mismatch. Two case studies are reported to illustrate the effect of Poisson's ratio.

6.2.1. Polymer Layer Sandwiched by Rigid Plates

An axisymmetric structure containing three layers of discs and the corresponding 2-D axisymmetric model are shown in Figure 6.6(a) and (b), respectively. Materials 1 and 2 represent a chip and a polymer layer. Their moduli and CTE are: 110 and 20 GPa and 3 and 20 ppm/°C for Material 1 and 2, respectively. In the analysis, a constant Poisson's ratio of 0.2 was used for Material 1 while the Poisson's ratio of Material 2 varied from 0.2 to 0.45.

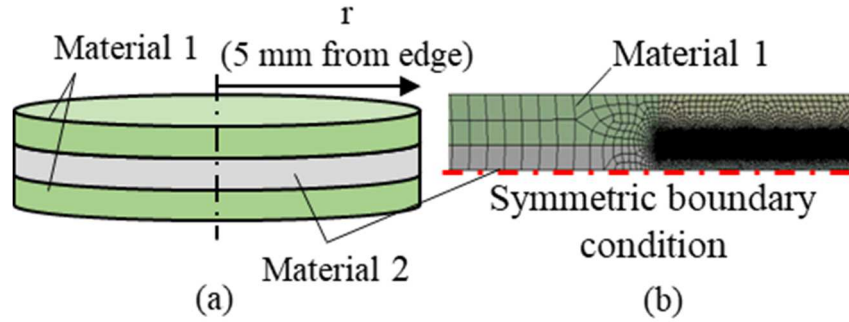


Figure 6.6 Axisymmetric structure containing three layers of discs and (b) the corresponding 2-D axisymmetric model

The model is subjected to a thermal loading of 80 °C. The axial stress, which is the stress normal to the material interface at the edge is the common cause of the failure of bonded materials. The axial stress distribution along the radial direction is shown in Figure 6.7. A very fine mesh near the interface around the edge was used to capture the singular stresses.

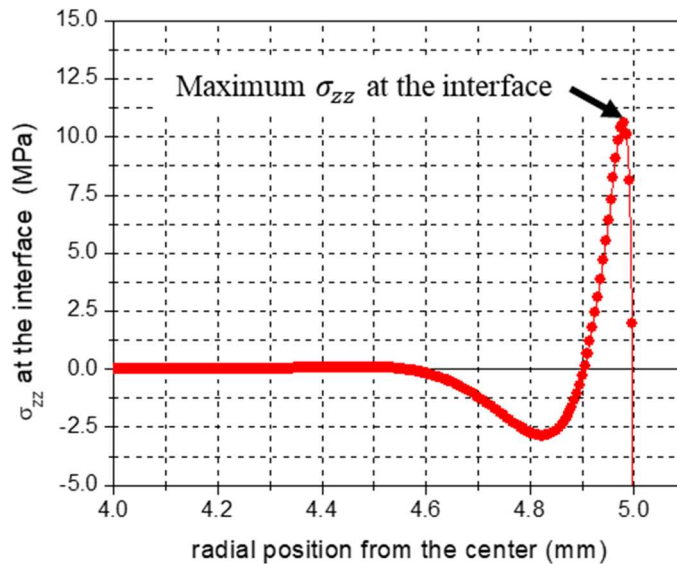


Figure 6.7 Axial stress along the interface

The maximum opening stresses were calculated while varying the Poisson's ratios of the polymer from 0.2 to 0.45, which represents the Poisson's ratio of typical filled thermosetting polymers. The results are shown in Figure 6.8

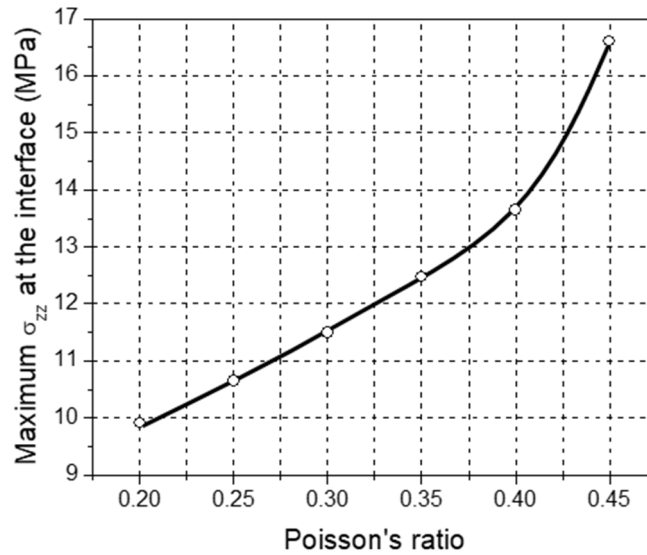


Figure 6.8 Maximum opening stress as a function of Poisson's ratio of Material 2

The maximum opening stress with the Poisson's ratio of 0.45 is about 50.9 % higher than the value with the Poisson's ratio of 0.20, which is significant when an interfacial failure is to be considered.

6.2.2. Wirebond Ball Grid Array (BGA) Package

A wirebond BGA package was used to investigate the effect of the Poisson's ratio on package warpage. The cross-sectional view of the package is shown schematically in Figure 6.9. It has two stacked dies over-molded by an epoxy molding compound (EMC). The quarter-symmetry was exploited in the numerical analysis. The numerical model is shown in Figure 6.10, where the geometry without EMC is shown in (a) and the actual mesh of the model is shown in (b).

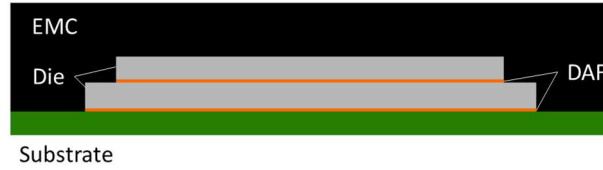


Figure 6.9 Cross-sectional view of the package

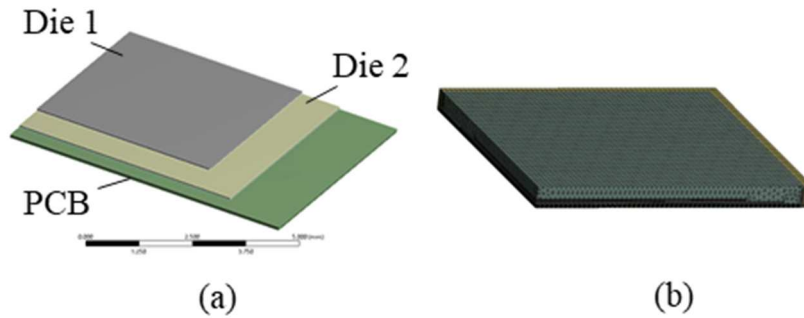
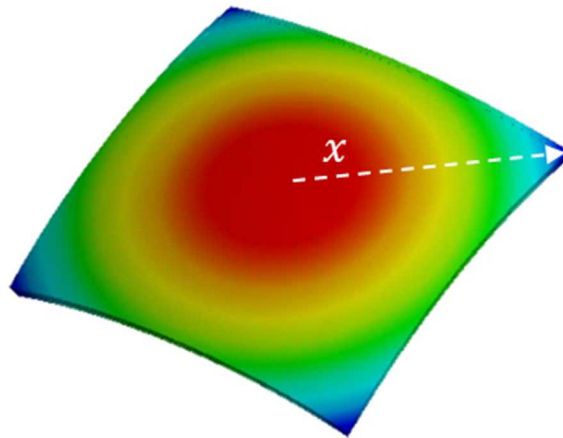


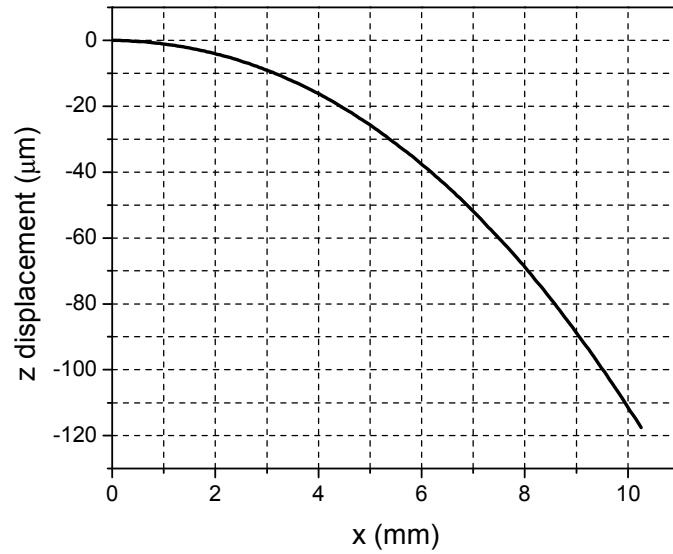
Figure 6.10 Quarter symmetric model of the package (a) geometry without EMC and (b) actual FEM mesh

In order to estimate the warpage during reflow, the package was heated from the transfer mold temperature of 175 °C to the reflow peak temperature of 240 °C. The deformed configuration is shown in Figure 6.11(a). The z-direction displacement along the diagonal direction is plotted in Figure 6.11 (b), from which the warpage is defined as the maximum relative z-displacement.

The warpage of the package was calculated as a function of Poisson's ratio of EMC. The results are shown in Figure 6.12. The warpage increases from 112.0 μm to 138.8 μm when the Poisson's ratio of EMC changes from 0.2 to 0.45. This change is significant (about 24% increase), and a correct Poisson's ratio should be used for accurate warpage prediction.



(a)



(b)

Figure 6.11 (a) Deformed configuration of the package and (b) the z displacement along the diagonal direction

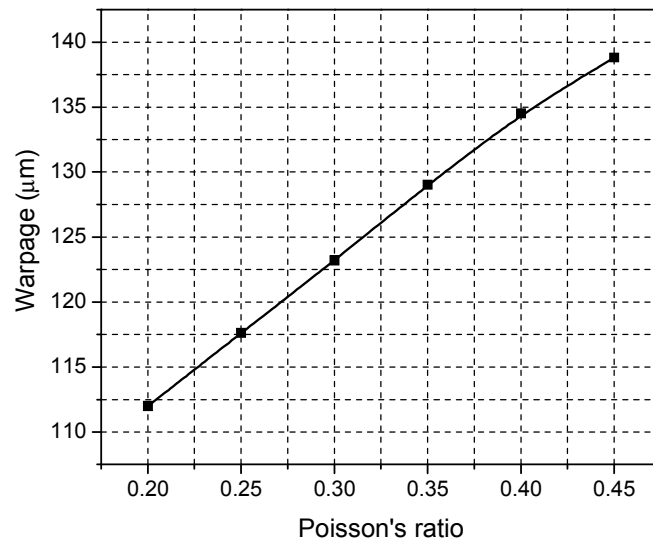


Figure 6.12 Warpage of the wire bond package as a function of Poisson's ratio of
EMC

Chapter 7 Conclusion and Future Work

7.1. Conclusion

An integrated measurement technique based on fiber Bragg grating (FBG) sensors was proposed and implemented to measure the viscoelastic properties of polymeric materials for accurate thermal stress analysis. The most significant contributions made in this dissertation are summarized below:

- a) A measurement technique to measure two time-temperature dependent elastic moduli was developed. Two time-dependent moduli were measured utilizing a single FBG embedded cylindrical specimen using two types of loading conditions.
- b) A sequential iterative procedure was developed to completely negate the effect of measurement uncertainties during complex non-linear regression.
- c) Three test setups, based on pneumatic systems, were developed: (1) to fabricate FBG embedded cylindrical specimen; to apply (2) uniaxial loading and (3) hydrostatic loading. Loading rates higher than those that the conventional mechanical testing machines were achieved using Air and He gas, which was critically required for accurate creep testing.
- d) A complete set of viscoelastic properties was obtained:

$$E(T,t), \nu(T,t), G(T,t) \text{ and } K(T,t)$$

- e) The effect of two widely practiced assumptions (a time and temperature independent bulk relaxation modulus for a viscoelastic analysis; and a constant Poisson's ratio for a linear elastic analysis) on the thermal stress

analysis of packages was investigated. The results clearly showed that the assumptions could overestimate thermal deformations significantly, especially when multi-axial constraints existed.

7.2. Future Work

The testing setups and the cylindrical FBG embedded specimen can be used to characterize other important properties.

a) Property degradation

One of the important advantages of the FBG is its robustness because it is fabricated on a glass fiber; it will not degrade unlike other conventional sensor such as a strain gage. Therefore, the setup and the specimen developed in this dissertation can be used to measure long-term degradation of polymers under harsh environmental conditions (e.g., temperature, UV exposure, humidity, etc.).

b) Cure extent dependent viscoelasticity

In order to determine the warpage and residual stress evolutions during curing, the cure extent dependent viscoelasticity would be required. The specimen configuration developed in this dissertation can be utilized to fabricate specimens as a function cure extent. Then the setups can be implemented to measure the cure extent dependent viscoelastic properties.

Reference

- [1] D. Lu and C. Wong, *Materials for advanced packaging* vol. 181: Springer, 2009.
- [2] C. Ober and G. Barclay, "Liquid Crystalline Thermosets As Materials For Microelectronics," *MRS Online Proceedings Library Archive*, vol. 227, 1991.
- [3] M. H. Meuwissen, H. A. de Boer, H. L. Steijvers, P. J. Schreurs, and M. G. Geers, "Residual stresses in microelectronics induced by thermoset packaging materials during cure," *Microelectronics Reliability*, vol. 44, pp. 1985-1994, 2004.
- [4] F. Pacheco-Torgal, R. Melchers, N. de Belie, X. Shi, K. Van Tittelboom, and A. S. Perez, *Eco-efficient repair and rehabilitation of concrete infrastructures*: Woodhead Publishing, 2017.
- [5] M. Jawaid, M. Thariq, and N. Saba, *Mechanical and physical testing of biocomposites, fibre-reinforced composites and hybrid composites*: Woodhead Publishing, 2018.
- [6] P. W. Beaumont, C. H. Zweben, E. Gdutos, R. Talreja, A. Poursartip, T. W. Clyne, M. B. Ruggles-Wrenn, T. Peijs, E. T. Thostenson, and R. Crane, *Comprehensive Composite Materials II*: Elsevier, 2018.
- [7] H. Ardebili, J. Zhang, and M. M. Pecht, *Encapsulation technologies for electronic applications*: William Andrew, 2018.
- [8] Available: https://ase.aseglobal.com/en/products/assembly_offerings
- [9] N. Kinjo, M. Ogata, K. Nishi, A. Kaneda, and K. Dušek, "Epoxy molding compounds as encapsulation materials for microelectronic devices," in *Speciality Polymers/Polymer Physics*, ed: Springer, 1989, pp. 1-48.
- [10] L. Turng and V. Wang, "On the simulation of microelectronic encapsulation with epoxy molding compound," *Journal of reinforced plastics and composites*, vol. 12, pp. 506-519, 1993.
- [11] W. Kim, J. W. Bae, I. D. Choi, and Y. S. Kim, "Thermally conductive EMC (epoxy molding compound) for microelectronic encapsulation," *Polymer Engineering & Science*, vol. 39, pp. 756-766, 1999.
- [12] T. Braun, S. Raatz, S. Voges, R. Kahle, V. Bader, J. Bauer, K.-F. Becker, T. Thomas, R. Aschenbrenner, and K.-D. Lang, "Large area compression molding for fan-out panel level packaging," in *2015 IEEE 65th Electronic Components and Technology Conference (ECTC)*, 2015, pp. 1077-1083.
- [13] C.-T. Ko, H. Yang, J. Lau, M. Li, M. Li, C. Lin, J. Lin, C.-L. Chang, J.-Y. Pan, and H.-H. Wu, "Design, materials, process, and fabrication of fan-out panel-level heterogeneous integration," *Journal of Microelectronics and Electronic Packaging*, vol. 15, pp. 141-147, 2018.
- [14] T. Braun, M. Topper, and S. Raatz, "Opportunities and Challenges for Fan-Out Panel Level Packaging (FOPLP)," *SiP Global Summit*, 2015.
- [15] J. H. Lau, M. Li, D. Tian, N. Fan, E. Kuah, W. Kai, M. Li, J. Hao, Y. M. Cheung, and Z. Li, "Warpage and thermal characterization of fan-out wafer-level packaging," *IEEE Transactions on Components, Packaging and Manufacturing Technology*, vol. 7, pp. 1729-1738, 2017.
- [16] Y. Oi, Y. Fujii, T. Hiraoka, Y. Yada, and K. Kan, "Warpage control of liquid molding compound for fan-out wafer level packaging," in *2018 IEEE 68th*

- Electronic Components and Technology Conference (ECTC)*, 2018, pp. 967-972.
- [17] M. Joshi, R. Pendse, V. Pandey, T. Lee, I. Yoon, J. Yun, Y. Kim, and H. Lee, "Molded underfill (MUF) technology for flip chip packages in mobile applications," in *2010 Proceedings 60th Electronic Components and Technology Conference (ECTC)*, 2010, pp. 1250-1257.
- [18] M. Azmi, M. Abdullah, M. Abdullah, Z. Ariff, A. A. Saad, M. Hamid, and M. Ismail, "Molded underfill (MUF) encapsulation for flip-chip package: A numerical investigation," in *AIP Conference Proceedings*, 2017, p. 040001.
- [19] T. Saito, T. Kitajima, M. Kawaguchi, S. Tajima, and M. Okamoto, "New Molding Technology Enabling Advanced Packaging Technology," in *2020 IEEE 70th Electronic Components and Technology Conference (ECTC)*, 2020, pp. 1957-1963.
- [20] K. Oota and M. Saka, "Cure shrinkage analysis of epoxy molding compound," *Polymer Engineering & Science*, vol. 41, pp. 1373-1379, 2001.
- [21] "Impact of Green Mold Compounds on First-and Second-Level Interconnect Reliability," 2013.
- [22] G. Kelly, C. Lyden, W. Lawton, J. Barrett, A. Saboui, H. Pape, and H. J. Peters, "Importance of molding compound chemical shrinkage in the stress and warpage analysis of PQFPs," *Components, Packaging, and Manufacturing Technology, Part B: Advanced Packaging, IEEE Transactions on*, vol. 19, pp. 296-300, 1996.
- [23] T. Y. Tee and Z. Zhong, "Integrated vapor pressure, hygroswelling, and thermo-mechanical stress modeling of QFN package during reflow with interfacial fracture mechanics analysis," *Microelectronics Reliability*, vol. 44, pp. 105-114, 2004.
- [24] J. W. Kong, J.-K. Kim, and M. M. Yuen, "Warpage in plastic packages: effects of process conditions, geometry and materials," *Electronics Packaging Manufacturing, IEEE Transactions on*, vol. 26, pp. 245-252, 2003.
- [25] K. Mahan, Y. Sun, B. Han, S. Han, and M. Osterman, "Adhesion and Puncture Strength of Polyurethane Coating Used to Mitigate Tin Whisker Growth," *Journal of electronic packaging*, vol. 136, p. 031004, 2014.
- [26] M.-Y. Tsai, Y.-C. Chen, and S. R. Lee, "Correlation between measurement and simulation of thermal warpage in PBGA with consideration of molding compound residual strain," *Components and Packaging Technologies, IEEE Transactions on*, vol. 31, pp. 683-690, 2008.
- [27] L. Li, K. Hubbard, and J. Xue, "Improving board assembly yield through PBGA warpage reduction," in *Electronic Packaging Technology & High Density Packaging, 2009. ICEPT-HDP'09. International Conference on*, 2009, pp. 949-953.
- [28] J. Kim, S. Lee, J. Lee, S. Jung, and C. Ryu, "Warpage Issues and Assembly Challenges Using Coreless Package Substrate."
- [29] X. Wang, Y. Andriani, S. Liu, Z. Chen, and X. Zhang, "Dynamic Mechanical Analysis and Viscoelastic Behavior of Epoxy Molding Compounds Used in Fan-Out Wafer-Level Packaging," in *2018 IEEE 20th Electronics Packaging Technology Conference (EPTC)*, 2018, pp. 585-590.

- [30] S.-S. Yeh, P.-Y. Lin, K.-C. Lee, J.-H. Wang, W.-Y. Lin, M.-C. Yew, P.-C. Lai, S.-T. Leu, and S.-P. Jeng, "Warpage modeling and characterization of the viscoelastic relaxation for cured molding process in fan-out packages," in *2017 IEEE 67th Electronic Components and Technology Conference (ECTC)*, 2017, pp. 841-846.
- [31] N. G. McCrum, C. Buckley, C. B. Bucknall, and C. Bucknall, *Principles of polymer engineering*: Oxford University Press, USA, 1997.
- [32] D. Roylance, "Engineering viscoelasticity," *Department of Materials Science and Engineering—Massachusetts Institute of Technology, Cambridge MA*, vol. 2139, pp. 1-37, 2001.
- [33] F. X. Che, M. Kawano, M. Z. Ding, Y. Han, and S. Bhattacharya, "Study on low warpage and high reliability for large package using TSV-free interposer technology through SMART codesign modeling," *IEEE Transactions on Components, Packaging and Manufacturing Technology*, vol. 7, pp. 1774-1785, 2017.
- [34] C.-H. Liu, L.-Y. Chen, C.-L. Lu, H.-C. Chen, C.-Y. Chen, and S.-C. Chang, "Wafer form warpage characterization based on composite factors including passivation films, Re-distribution layers, Epoxy molding compound utilized in innovative fan-out package," in *2017 IEEE 67th Electronic Components and Technology Conference (ECTC)*, 2017, pp. 847-852.
- [35] F. X. Che, K. Yamamoto, V. S. Rao, and V. N. Sekhar, "Panel Warpage of Fan-Out Panel-Level Packaging Using RDL-First Technology," *IEEE Transactions on Components, Packaging and Manufacturing Technology*, vol. 10, pp. 304-313, 2019.
- [36] L. Ernst, G. Zhang, K. Jansen, and H. Bressers, "Time-and temperature-dependent thermo-mechanical modeling of a packaging molding compound and its effect on packaging process stresses," *Journal of Electronic Packaging*, vol. 125, pp. 539-548, 2003.
- [37] D. J. O'Brien, N. Sottos, and S. R. White, "Cure-dependent viscoelastic Poisson's ratio of epoxy," *Experimental mechanics*, vol. 47, pp. 237-249, 2007.
- [38] M. Sadeghinia, K. Jansen, and L. Ernst, "Characterization and modeling the thermo-mechanical cure-dependent properties of epoxy molding compound," *International Journal of Adhesion and Adhesives*, vol. 32, pp. 82-88, 2012.
- [39] I. Emri and T. Prodan, "A measuring system for bulk and shear characterization of polymers," *Experimental mechanics*, vol. 46, pp. 429-439, 2006.
- [40] W. Van Driel, J. Janssen, G. Zhang, D. Yang, and L. Ernst, "Packaging Induced Die Stresses—Effect of Chip Anisotropy and Time-Dependent Behavior of a Molding Compound," *Journal of Electronic Packaging*, vol. 125, pp. 520-526, 2003.
- [41] S.-H. Chae, J.-H. Zhao, D. R. Edwards, and P. S. Ho, "Characterization of Viscoelasticity of Molding Compounds in Time Domain," in *ASME 2009 InterPACK Conference collocated with the ASME 2009 Summer Heat Transfer Conference and the ASME 2009 3rd International Conference on Energy Sustainability*, 2009, pp. 435-441.

- [42] J. Liang, R. Li, and S. Tjong, "Effects of glass bead size and content on the viscoelasticity of filled polypropylene composites," *Polymer testing*, vol. 19, pp. 213-220, 2000.
- [43] R. Hagen, L. Salmén, H. Lavebratt, and B. Stenberg, "Comparison of dynamic mechanical measurements and T_g determinations with two different instruments," *Polymer testing*, vol. 13, pp. 113-128, 1994.
- [44] D.-L. Chen, P.-F. Yang, and Y.-S. Lai, "A review of three-dimensional viscoelastic models with an application to viscoelasticity characterization using nanoindentation," *Microelectronics Reliability*, vol. 52, pp. 541-558, 2012.
- [45] H. F. Brinson and L. C. Brinson, *Polymer engineering science and viscoelasticity*: Springer, 2008.
- [46] J. de Vreugd, K. Jansen, A. Xiao, L. Ernst, C. Bohm, A. Kessler, H. Preu, and M. Stecher, "Advanced viscoelastic material model for predicting warpage of a QFN panel," in *Electronic Components and Technology Conference, 2008. ECTC 2008. 58th*, 2008, pp. 1635-1640.
- [47] S.-S. Yeh, P.-Y. Lin, K.-C. Lee, J.-H. Wang, W.-Y. Lin, M.-C. Yew, P.-C. Lai, C.-K. Hsu, C.-C. Yang, and S.-P. Jeng, "Fan-out wafer molding process optimization using cure-dependent viscoelastic modeling and characterizations," in *2017 12th International Microsystems, Packaging, Assembly and Circuits Technology Conference (IMPACT)*, 2017, pp. 148-151.
- [48] J. McPherson, "Brief history of JEDEC qualification standards for silicon technology and their applicability (?) to WBG semiconductors," in *2018 IEEE International Reliability Physics Symposium (IRPS)*, 2018, pp. 3B. 1-1-3B. 1-8.
- [49] C. Prasad, S. Chugh, H. Greve, I.-c. Ho, E. Kabir, C. Lin, M. Maksud, S. R. Novak, B. Orr, and K. W. Park, "Silicon Reliability Characterization of Intel's Foveros 3D Integration Technology for Logic-on-Logic Die Stacking," in *2020 IEEE International Reliability Physics Symposium (IRPS)*, 2020, pp. 1-5.
- [50] N. Vijayaragavan, F. Carson, and A. Mistry, "Package on Package warpage-impact on surface mount yields and board level reliability," in *Electronic Components and Technology Conference, 2008. ECTC 2008. 58th*, 2008, pp. 389-396.
- [51] P. Sun, V. C.-K. Leung, B. Xie, V. W. Ma, and D. X.-Q. Shi, "Warpage reduction of package-on-package (PoP) module by material selection & process optimization," in *Electronic Packaging Technology & High Density Packaging, 2008. ICEPT-HDP 2008. International Conference on*, 2008, pp. 1-6.
- [52] Y. L. Tzeng, N. Kao, E. Chen, J. Y. Lai, Y. P. Wang, and C. Hsiao, "Warpage and stress characteristic analyses on package-on-package (POP) structure," in *Electronics Packaging Technology Conference, 2007. EPTC 2007. 9th*, 2007, pp. 482-487.
- [53] G. Caswell, "Challenges With Package on Package (PoP) Technology," 2012.
- [54] H. Jeong, K.-H. Jung, C.-J. Lee, K. D. Min, W.-R. Myung, and S.-B. Jung, "Effect of epoxy mold compound and package dimensions on the thermomechanical properties of a fan-out package," *Journal of Materials Science: Materials in Electronics*, pp. 1-8, 2020.

- [55] T. A. Osswald and G. Menges, *Materials science of polymers for engineers*: Carl Hanser Verlag GmbH Co KG, 2012.
- [56] A. F. Lewis, "Dynamic mechanical behavior during the thermosetting curing process," *Polymer Engineering & Science*, vol. 3, pp. 201-209, 1963.
- [57] Y. Wang, B. Han, D. Kim, A. Bar-Cohen, and P. Joseph, "Integrated measurement technique for curing process-dependent mechanical properties of polymeric materials using fiber bragg grating," *Experimental mechanics*, vol. 48, pp. 107-117, 2008.
- [58] F. Su, L. Liu, and T. Wang, "Evaluation of Residual Stress in Flip Chip Using 3-D Optical Interferometry/FEM Hybrid Technique," *Strain*, vol. 43, pp. 289-298, 2007.
- [59] M.-Y. Tsai, C. J. Hsu, and C. O. Wang, "Investigation of thermomechanical behaviors of flip chip BGA packages during manufacturing process and thermal cycling," *IEEE Transactions on Components and Packaging Technologies*, vol. 27, pp. 568-576, 2004.
- [60] M.-Y. Tsai, Y.-C. Lin, C.-Y. Huang, and J.-D. Wu, "Thermal deformations and stresses of flip-chip BGA packages with low-and high-T/sub g/underfills," *IEEE transactions on electronics packaging manufacturing*, vol. 28, pp. 328-337, 2005.
- [61] Y. Sun, Y. Wang, C. Jang, B. Han, and K. Choi, "Generalized Hybrid Modeling to Determine Chemical Shrinkage and Modulus Evolutions at Arbitrary Temperatures," *Experimental mechanics*, pp. 1-8, 2013.
- [62] A. Spoelstra, G. Peters, and H. Meijer, "Chemorheology of a highly filled epoxy compound," *Polymer Engineering & Science*, vol. 36, pp. 2153-2162, 1996.
- [63] K. I. Y. Chien, J. Zhang, L. Rector, and M. Todd, "Low Warpage Molding Compound Development for Array Packages," in *Electronics Systemintegration Technology Conference, 2006. 1st*, 2006, pp. 1001-1006.
- [64] S.-S. Deng, S.-J. Hwang, and H.-H. Lee, "Warpage Prediction and Experiments of Fan-Out Waferlevel Package During Encapsulation Process," 2013.
- [65] H. Ishida and H. Y. Low, "A study on the volumetric expansion of benzoxazine-based phenolic resin," *Macromolecules*, vol. 30, pp. 1099-1106, 1997.
- [66] S. J. Hwang and Y. S. Chang, "Isobaric cure shrinkage behaviors of epoxy molding compound in isothermal state," *Journal of Polymer Science Part B: Polymer Physics*, vol. 43, pp. 2392-2398, 2005.
- [67] V. Fano, I. Ortalli, S. Pizzi, and M. Bonanini, "Polymerization shrinkage of microfilled composites determined by laser beam scanning," *Biomaterials*, vol. 18, pp. 467-470, 1997.
- [68] A. W. Snow and J. P. Armistead, "A simple dilatometer for thermoset cure shrinkage and thermal expansion measurements," *Journal of applied polymer science*, vol. 52, pp. 401-411, 1994.
- [69] W. Cook, M. Forrest, and A. Goodwin, "A simple method for the measurement of polymerization shrinkage in dental composites," *Dental Materials*, vol. 15, pp. 447-449, 1999.
- [70] C. L. Thomas and A. J. Bur, "In-situ monitoring of product shrinkage during injection molding using an optical sensor," *Polymer Engineering & Science*, vol. 39, pp. 1619-1627, 1999.

- [71] A. Hudson, S. Martin, M. Hubert, and J. Spelt, "Optical measurements of shrinkage in UV-cured adhesives," *Journal of electronic packaging*, vol. 124, pp. 352-354, 2002.
- [72] H. Yu, S. Mhaisalkar, and E. Wong, "Cure shrinkage measurement of nonconductive adhesives by means of a thermomechanical analyzer," *Journal of electronic materials*, vol. 34, pp. 1177-1182, 2005.
- [73] D. Karalekas, I. M. Daniel, J. T. Gotro, and T.-M. Wang, "Determination of chemical cure shrinkage in composite laminates," *Journal of Composites, Technology and Research*, vol. 12, pp. 172-176, 1990.
- [74] A. A. Stolov, T. Xie, J. Penelle, and S. L. Hsu, "Simultaneous measurement of polymerization kinetics and stress development in radiation-cured coatings: A new experimental approach and relationship between the degree of conversion and stress," *Macromolecules*, vol. 33, pp. 6970-6976, 2000.
- [75] W. Zhu, G. Li, W. Sun, F. Che, A. Sun, C. Wang, H. Tan, B. Zhao, and N. Chin, "Cure shrinkage characterization and its implementation into correlation of warpage between simulation and measurement," in *Thermal, Mechanical and Multi-Physics Simulation Experiments in Microelectronics and Micro-Systems, 2007. EuroSime 2007. International Conference on*, 2007, pp. 1-8.
- [76] K. Jansen, J. de Vreugd, and L. Ernst, "Analytical estimate for cure-induced stresses and warpage in flat packages," in *Thermal, Mechanical and Multi-Physics Simulation and Experiments in Microelectronics and Microsystems (EuroSimE), 2011 12th International Conference on*, 2011, pp. 1/4-4/4.
- [77] G. Hu, S. Chew, and J.-E. Luan, "Characterization of chemical cure shrinkage of epoxy molding compound with application to warpage analysis," *Journal of electronic packaging*, vol. 131, p. 011010, 2009.
- [78] C. Li, K. Potter, M. R. Wisnom, and G. Stringer, "In-situ measurement of chemical shrinkage of MY750 epoxy resin by a novel gravimetric method," *Composites Science and Technology*, vol. 64, pp. 55-64, 2004.
- [79] J. Lange, S. Toll, J.-A. E. Månson, and A. Hult, "Residual stress build-up in thermoset films cured above their ultimate glass transition temperature," *Polymer*, vol. 36, pp. 3135-3141, 1995.
- [80] K. Kim and H. Hahn, "Residual stress development during processing of graphite/epoxy composites," *Composites Science and Technology*, vol. 36, pp. 121-132, 1989.
- [81] T. Curiel and G. Fernlund, "Deformation and stress build-up in bi-material beam specimens with a curing FM300 adhesive interlayer," *Composites part A: applied science and manufacturing*, vol. 39, pp. 252-261, 2008.
- [82] K. M. Jansen, C. Qian, L. J. Ernst, C. Bohm, A. Kessler, H. Preu, and M. Stecher, "Modeling and characterization of molding compound properties during cure," *Microelectronics Reliability*, vol. 49, pp. 872-876, 2009.
- [83] K. Jansen, L. Wang, D. Yang, C. van't Hof, L. Ernst, H. Bressers, and G. Zhang, "Constitutive modeling of moulding compounds [electronic packaging applications]," in *Electronic Components and Technology Conference, 2004. Proceedings. 54th*, 2004, pp. 890-894.

- [84] C. T. McKee, J. A. Last, P. Russell, and C. J. Murphy, "Indentation versus tensile measurements of Young's modulus for soft biological tissues," *Tissue Engineering Part B: Reviews*, vol. 17, pp. 155-164, 2011.
- [85] J. De Vreugd, K. M. Jansen, L. J. Ernst, and C. Bohm, "Prediction of cure induced warpage of micro-electronic products," *Microelectronics Reliability*, vol. 50, pp. 910-916, 2010.
- [86] S. L. Simon, G. B. McKenna, and O. Sindt, "Modeling the evolution of the dynamic mechanical properties of a commercial epoxy during cure after gelation," *Journal of applied polymer science*, vol. 76, pp. 495-508, 2000.
- [87] M. Zarrelli, I. K. Partridge, and A. D'Amore, "Warpage induced in bi-material specimens: Coefficient of thermal expansion, chemical shrinkage and viscoelastic modulus evolution during cure," *Composites part A: applied science and manufacturing*, vol. 37, pp. 565-570, 2006.
- [88] Y. K. Kim and S. R. White, "Stress relaxation behavior of 3501 □ 6 epoxy resin during cure," *Polymer Engineering & Science*, vol. 36, pp. 2852-2862, 1996.
- [89] Y.-J. Lin, S.-J. Hwang, H.-H. Lee, and D.-Y. Huang, "Modeling of viscoelastic behavior of an epoxy molding compound during and after curing," *Components, Packaging and Manufacturing Technology, IEEE Transactions on*, vol. 1, pp. 1755-1760, 2011.
- [90] E. A. Campo, *Selection of polymeric materials: how to select design properties from different standards*: William Andrew, 2008.
- [91] E. Riande, R. Diaz-Calleja, M. Prolongo, R. Masegosa, and C. Salom, *Polymer viscoelasticity: stress and strain in practice*: CRC Press, 1999.
- [92] J. Bicerano, *Prediction of polymer properties*: cRc Press, 2002.
- [93] A. Amirkhizi, J. Isaacs, J. McGee, and S. Nemat-Nasser, "An experimentally-based viscoelastic constitutive model for polyurea, including pressure and temperature effects," *Philosophical magazine*, vol. 86, pp. 5847-5866, 2006.